

Mathematical modelling and numerical simulations of actin dynamics in the eukaryotic cell

Uduak Z. George · Angélique Stéphanou ·
Anotida Madzvamuse

Received: 1 August 2011 / Revised: 2 December 2011 / Published online: 21 March 2012
© Springer-Verlag 2012

Abstract The aim of this article is to study cell deformation and cell movement by considering both the mechanical and biochemical properties of the cortical network of actin filaments and its concentration. Actin is a polymer that can exist either in filamentous form (F-actin) or in monomeric form (G-actin) (Chen et al. in *Trends Biochem Sci* 25:19–23, 2000) and the filamentous form is arranged in a paired helix of two protofilaments (Ananthakrishnan et al. in *Recent Res Devel Biophys* 5:39–69, 2006). By assuming that cell deformations are a result of the cortical actin dynamics in the cell cytoskeleton, we consider a continuum mathematical model that couples the mechanics of the network of actin filaments with its bio-chemical dynamics. Numerical treatment of the model is carried out using the moving grid finite element method (Madzvamuse et al. in *J Comput Phys* 190:478–500, 2003). Furthermore, by assuming slow deformations of the cell, we use linear stability theory to validate the numerical simulation results close to bifurcation points. Far from bifurcation points, we show that the mathematical model is able to describe the complex cell deformations typically observed in experimental results. Our numerical results illustrate cell expansion, cell contraction, cell translation and cell relocation as well as cell protrusions. In all these results, the contractile tonicity formed by the association of actin filaments to the myosin II motor proteins is identified as a key bifurcation parameter.

U. Z. George (✉) · A. Madzvamuse
Department of Mathematics, University of Sussex, Brighton BN1 9QH, UK
e-mail: U.Z.George@sussex.ac.uk

A. Madzvamuse
e-mail: a.madzvamuse@sussex.ac.uk

A. Stéphanou
DyCTiM Research Team, UJF-Grenoble 1, CNRS,
Laboratoire TIMC-IMAG UMR 5525,
38041 Grenoble, France

Keywords Actin dynamics · Cell deformation · Moving grid finite element · Lagrangian kinematics

Mathematics Subject Classification 74L15 · 74S05 · 74F25 · 92C17

1 Introduction

Cells are usually minute in size but complex in structure and dynamics. They are the smallest known basic unit of life and are capable of existing on their own in the form of a single cell organism such as amoeba. They can also exist as a group of cells (as found in multicellular organisms such as slime molds) working together to perform specific tasks towards the well being or detriment of the organism. They perform some cellular functions by responding to stimuli in their environment. Usually by becoming polarised, moving, deforming (i.e a change in shape or size) and repositioning their intracellular organelles (Chen et al. 2000). Likewise in the absence of external stimuli, cells in vitro are found to deform spontaneously (Maeda et al. 2008; Binamé et al. 2010). It is now well established that the cortical actin filaments play an important part in both the spontaneous and migratory behaviour of cells, though the series of events that lead to each may be different (Stephanou et al. 2004).

The migratory behaviour of cells plays a crucial role in many biological events [e.g. physiological and pathological process (Le Clainche and Carlier 2008)] such as immune response (Ridley et al. 2003; Fleischer et al. 2007; Lauffenburgy and Horwitz 1996), wound healing, development of tissues (Xue et al. 2010), embryogenesis (Stephanou 2010; Clark 1996), inflammation and the formation of tumour metastasis (Stéphanou et al. 2008; Lauffenburgy and Horwitz 1996). A significant amount of work has been done in determining the migratory behaviour of cells. Most of this work has been done through theoretical studies, laboratory experiments and mathematical modelling of cell dynamics (Zaman et al. 2005). In the last few decades, a lot of studies were carried out in order to aid the understanding of biochemical processes of cell motility. These studies have improved our understanding of the order of events and the identification of some key molecular components that are actively involved in cell motility (Keren and Theriot 2008). Migration is the result of a cycle of multistep events (Xue et al. 2010) namely: protrusion of pseudopodia in front of the cell body (the protrusion must be large for migration to be sustained), the formation of new adhesion sites that connect the extracellular matrix to the actin cytoskeleton at the protrusion regions (Le Clainche and Carlier 2008), the development of traction, translocation of the cell body and the release of old adhesion sites at the rear of the cell (Lauffenburgy and Horwitz 1996; Gupton et al. 2005; Ananthakrishnan and Ehrlicher 2007). These events depend on the mechanical properties of the cells which in turn are determined by the cytoskeleton and its associated proteins, cell structures as well as the surroundings with which the cells interact (Zhu et al. 2000). On the contrary, less work has been done towards the understanding of the spontaneous deformation of cells (Stephanou et al. 2004). Spontaneous deformation is found to occur in both static and motile cells (Maeda et al. 2008). It has been hypothesised that spontaneous deformation of a cell is caused by an internal pressure generated in the cell cytoplasm

as a result of the cortical actomyosin contraction. This pressure is assumed to be sufficient in pushing the cell membrane outward at positions where the membrane is not strongly linked to the cytoskeleton (Binamé et al. 2010; Paluch et al. 2005, 2006). It is clear that any work geared towards understanding the spontaneous dynamics of cells would aid shed more light on the mechanisms that govern cell dynamics and also improve understanding of the mechanisms and processes that prompt a static cell to begin to migrate.

Most of the recent studies on cell migration have focused on the mechanisms of cell-signalling that play a part towards the occurrence and sustenance of large-scale cell polarity while little attention has been given to the study of the mechanical and physical factors that engineer the large-scale coordination of cell dynamics (Keren and Theriot 2008). By coupling the interactions among the various mechanical and biochemical factors, a better understanding could be gained on the various cellular processes that regulate cell movement (Okeyo et al. 2009). Although there has been a considerable amount of work towards the study of the F-actin network dynamics, it is not fully understood how the mechanical forces produced by actomyosin contractility spatiotemporally control the F-actin flows and deformations (Okeyo et al. 2009). In Okeyo et al. (2009), it has been suggested that the mechanical forces originating from the actomyosin interactions are key to the occurrence of cell movement. Actin is a polymer that can exist either in filamentous form (F-actin) or in monomeric form (G-actin) (Chen et al. 2000) and F-actin is arranged in a paired helix of two protofilaments (Ananthakrishnan et al. 2006). The actin cortex is made up of short actin filaments that are arranged as a three-dimensional meshwork of approximately 50 nm (Ananthakrishnan et al. 2006) and underlies the cell membrane. The size of the meshwork increases towards the interior of the cell to approximately 300 nm (Ananthakrishnan et al. 2006). Actin filament usually undergoes rapid polymerisation (into F-actin) and depolymerisation (into G-actin) and this depends on physical or chemical conditions that influence the cell (Pullarkat and Fernández 2007). Its network is the most prevalent and dynamic protein in the cell cytoskeleton and plays an important part in maintaining cell shape and locomotion (Pullarkat and Fernández 2007).

The aim of this work is to study cell deformations by considering both the mechanical and biochemical properties of the cortical network of actin filaments and its concentration. In this study, we adopt the hypothesis that the filaments will either push on the membrane when they polymerise in order to create more space for the extension of actin filaments or pull on the membrane when they contract. Contraction of the filaments occurs as a result of the interaction of actin with myosin which is a protein found in the cytoplasm. As a result of the interaction between actin filaments and myosin-II, stress fibres generate a contractile force that is used in cell locomotion and control of cell shape (Senju and Miyata 2009; Bischofs et al. 2008). We also assumed that the contraction of the network creates cytoplasmic flows throughout the cell which increase the pressure in the cytoplasm and push the membrane outward at locations where the membrane is not firmly linked to the actin network (Stephanou et al. 2004).

Our model is a modification of a cytomechanical model by Stephanou et al. (2004) which was an extension of an earlier model describing the actin cytogel by Lewis and Murray (1991, 1992). In our model we focus on the polymerisation kinetics of actin

with regard to cell deformations as was done in [Stephanou et al. \(2004\)](#) and [Alt and Tranquillo \(1995\)](#).

A two-dimensional (2D) approximation of the problem holds since the cell that we consider is an in vitro cell adhering on a 2D substrate. In an experimental condition the lamellipodial zone where the actin dynamics are taking place is very flat and can be considered 2D. In [Stephanou et al. \(2004\)](#) the description of the actin dynamics was restricted to a one-dimensional circular active layer of radius r in order to avoid the problem involved in dealing with a free moving cell boundary with the boundary parameterised using a 2D polar coordinate system. The limitation of the polar coordinate system is its difficulty in describing the evolution of a domain as it moves outside the origin of the polar coordinate. These limitations can be dealt with by using a different computational model for its numerical approximation derived based on for example, a level set method (LSM) ([Sethian 1996](#)), a boundary element method (BEM) ([Brebbia 1981](#); [Crouch and Starfield 1983](#)) or a finite element method (FEM) ([Reddy 1993](#); [Zienkiewicz et al. 2005](#); [Madzvamuse et al. 2003](#)). BEM is an efficient numerical tool that is very useful in the discretization of models where only the surface is of interest ([Hofreither et al. 2010](#)). And it is computationally expensive to obtain solutions in the interior of the domain. Also the application of the BEM to second-order inhomogeneous partial differential equations and nonlinear problems is much more difficult compared to the FEM ([LaForce 2006](#)). Mathematical models that describe cell dynamics are usually non-linear in nature. FEM can be used easily to approximate non-linear problems and can handle continuously deforming complex geometries ([Reddy 1993](#); [Sadd 2005](#)) and are thus perfect for modelling cell deformations. The LSM is an efficient numerical technique that can be used to track the motion of complex fronts as they evolve ([Sethian 1996](#)). The LSM method will not be implemented here but we intend to use it in future studies to track splitting and reconnecting cells.

In view of these, we develop in this paper a finite element model that is defined in a 2D cartesian coordinate system. In Sect. 2 we introduce the model problem. Non-dimensionalization of the mathematical model is carried out in Sect. 3 in order to reduce the number of model parameters. Furthermore, in this section we carry out linear stability theory in order to identify key bifurcation parameters as well as compute analytical solutions close to bifurcation points that will be used to validate numerical results. We present the finite element numerical scheme for our model in Sect. 4 and in Sect. 5 we present our findings and show that this model is able to describe the intracellular actin dynamics and the resulting shapes and movements of protrusion and retraction of the membrane. Furthermore we highlight key parameters of the model that determine the cell membrane dynamics.

2 Model problem

The model problem for the actin dynamics is an extension of an existing mechano-chemical model which describes the actin cytosol ([Lewis and Murray 1991, 1992](#)). In the cytosol model, sol/gel transition kinetics were considered, in our case we focus on the polymerisation kinetics of actin as was done by [Stephanou et al. \(2004\)](#).

The network of actin filament is considered as a viscoelastic and contractile gel. These properties are represented by stress tensors comprising a viscous σ_v , elastic σ_e , contractile σ_c components, plus an additional pressure component σ_p . Actin is supposed to move under diffusion and convective effects. We assume that at the intra-cellular level, the cell complies to Newtonian dynamics such that inertial terms are negligible compared to viscous and elastic forces hence motion ceases as soon as the forces are turned off (Lewis and Murray 1991; Purcell 1977).

We consider the kinetics of polymerisation and depolymerization of actin filaments by assuming that the filaments either push on the membrane when they polymerise or pull on the membrane when tethered to it, by contracting. We also assume that the contraction of the network creates cytoplasmic flows throughout the cell which lead to an increased pressure. This pressure pushes the membrane outward at locations where the membrane is not firmly linked to the actin network. Thus the model consists of two coupled equations, a force balance equation (2.1a) that describes the mechanical properties of the network of interconnected actin filaments in the cell cytoplasm and a reaction–diffusion equation (2.1b) that describes the concentration of actin, its random movement via diffusion, convective and dilution effects due to shape movement and its kinetics of polymerisation and depolymerization.

Let $\Omega_t \subset \mathbb{R}^2$ be a simply connected bounded continuously deforming domain representing the cell shape at time $t \in I = [0, T_f]$, $T_f > 0$ and $\partial\Omega_t$ be the boundary describing the cell. At any given point, $\mathbf{x} = (x(t), y(t)) \in \Omega_t \subset \mathbb{R}^2$, let $a = a(\mathbf{x}(t), t)$ be the F-actin concentration and $\mathbf{u} = (u(\mathbf{x}(t), t), v(\mathbf{x}(t), t))^T$ be a vector of displacement of the elements of the actin network at position $\mathbf{x} \in \Omega_t$ at time $t \in I$. As a result of cell movement we define $\boldsymbol{\beta}$ to represent the flow velocity of the elements of the actin network and $\boldsymbol{\omega}_n$ the normal velocity of the boundary. Furthermore denote $\mathbf{n} = (n_x, n_y)$ the outward unit vector normal to the boundary. We note that by defining \mathbf{u} to be a vector of displacement of the elements of the actin network at position $\mathbf{x} \in \Omega_t$ at time $t \in I$, the following system of equations describing the actin dynamics as given by Stephanou et al. (2004) models both plasticity and viscoelasticity of the actin network:

$$\nabla \cdot (\sigma_v + \sigma_e + \sigma_c + \sigma_p) = \mathbf{0} \quad \text{in } \Omega_t, \quad t \in I, \quad (2.1a)$$

$$\frac{\partial a}{\partial t} - D_a \Delta a + \nabla \cdot (a\boldsymbol{\beta}) - k_a(a_c - a) = 0 \quad \text{in } \Omega_t, \quad t \in I, \quad (2.1b)$$

$$\mathbf{u}(\mathbf{x}(t), t) = \mathbf{0} \quad \text{for } \mathbf{x} \in \Omega_t, \quad t = 0, \quad (2.1c)$$

$$a(\mathbf{x}(t), t) = a_0 \quad \text{for } \mathbf{x} \in \Omega_t, \quad t = 0, \quad (2.1d)$$

$$\boldsymbol{\beta} = \boldsymbol{\omega}_n \quad \text{for } \mathbf{x} \in \partial\Omega_t, \quad t \in I, \quad (2.1e)$$

$$\sigma_v \cdot \mathbf{n} = \sigma_e \cdot \mathbf{n} = \mathbf{n} \cdot \nabla a = 0 \quad \text{for } \mathbf{x} \in \partial\Omega_t, \quad t \in I, \quad (2.1f)$$

where in (2.1a), σ_v , σ_e , σ_c and σ_p are the viscous, elastic, contractile and pressure component stress tensors. These are defined as:

$$\sigma_c = \sigma(a)\mathbf{I} = \psi a^2 e^{-a/a_{sat}} \mathbf{I}, \quad (2.2)$$

$$\sigma_v = \mu_1 \frac{\partial \epsilon}{\partial t} + \mu_2 \frac{\partial \phi}{\partial t} \mathbf{I}, \quad (2.3)$$

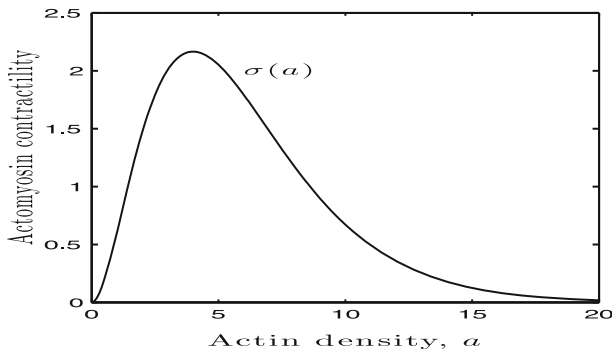


Fig. 1 Function $\sigma(a)$ describing the actomyosin network contractility. The contractility first increases in a parabolic way with the actin density until a critical density of actin is reached after which the contractility begins to decrease exponentially. This is due to compaction of the network which prevents further contraction. Here $a_{sat} = 1.1$ and $\psi = 1.0$

$$\sigma_e = \frac{E}{1+\nu} \left(\epsilon + \frac{\nu}{1-2\nu} \phi \mathbf{I} \right), \quad (2.4)$$

$$\sigma_p = \frac{p}{1+\phi} \left(1 + \frac{2}{\pi} \delta(l) \arctan a \right) \mathbf{I}, \quad (2.5)$$

where $\epsilon = \frac{1}{2}(\nabla \mathbf{u} + \nabla \mathbf{u}^T)$ is the strain tensor, \mathbf{I} is the identity tensor, $\phi = \nabla \cdot \mathbf{u}$ is the dilation, and μ_1 and μ_2 are the shear and bulk viscosities of the actin network respectively. Finally E and ν are the Young's modulus and Poisson ratio respectively. The function $\sigma(a)$ represents the contractile activity of the actomyosin network (see Fig. 1). In the above formulation, $2a_{sat}$ represents the saturation concentration of F-actin.

In order to describe the pressure forces acting within the cell we make the following assumptions. We assume that the initial domain is a unit disk which we denote as Ω_0 and that there exists a family of bijective mappings that maps the points $\xi = (\xi_x, \xi_y)$ of the initial domain to point \mathbf{x} on the current domain Ω_t . Let $l : \Omega_t \times I \rightarrow \mathcal{R}$ and it's corresponding function on the initial domain be $\hat{l} : \Omega_0 \times I \rightarrow [0, 1]$ where $\hat{l}(\xi, t)$ is the distance between the centroid and the point ξ in the initial domain with $\hat{l}(\xi, t) = l(\mathbf{x}(\xi, t), t)$. The function $p(a) := \frac{p}{1+\phi} (1 + \frac{2}{\pi} \delta(l) \arctan a)$ describes the pressure force in different regions governed by the heavy-side function:

$$\delta(l) = \begin{cases} 1 & \text{if the point } (\mathbf{x}, t) \text{ with } l(\mathbf{x}(\xi, t), t) = \hat{l}(\xi, t) \text{ is such that} \\ & \text{the distance } \sqrt{\xi_x^2 + \xi_y^2} > 0.8 \text{ in the initial domain,} \\ 0 & \text{elsewhere.} \end{cases} \quad (2.6)$$

This signifies that far from the membrane, only the osmotic component $p/(1+\phi)$ of the pressure force exists within the network and depends on the dilation ϕ . In the vicinity of the membrane (i.e. where $\sqrt{\xi_x^2 + \xi_y^2} > 0.8$), a polymerisation-induced pressure which depends on the local actin density reinforces the osmotic stress and pushes the

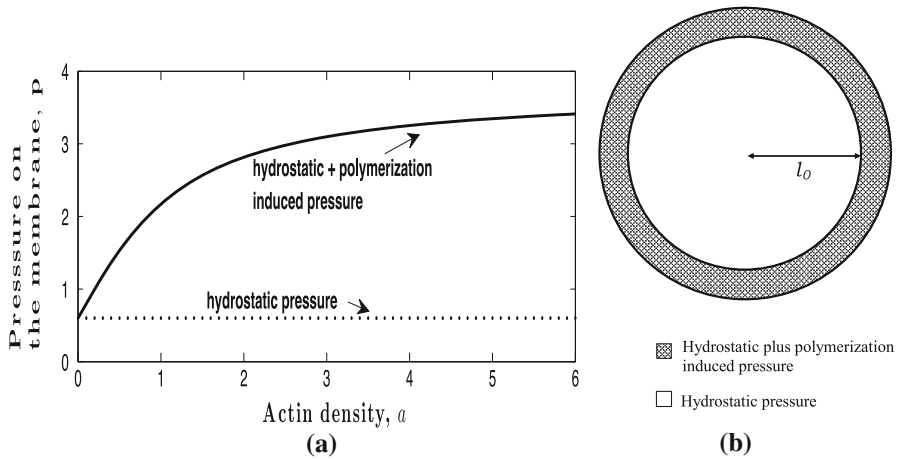


Fig. 2 A graphical and pictorial description of the variation of the function $p(a)$ on a typical cell. In **a** the function $p(a)$ is shown describing the pressure force existing at the vicinity of the membrane. This force comprises of a passive hydrostatic component and an active polymerization-induced force component corresponding to the force applied by the growing filaments pushing on the membrane to create the space required for their growth. In **b** a schematic illustration of the variation of the function $p(a)$ within a typical cell is shown, where $l_0 = 0.8$

membrane out at regions where the filaments are not firmly linked to the membrane (see Fig. 2 for a graphical illustration). $\delta(l)$ is used here to specify the differences in pressure in the cell at the vicinity of the membrane and further away from it. We have assumed that the polymerisation of actin, which happens predominately at the vicinity of the membrane, induces a pressure that reinforces the osmotic pressure at the vicinity of the membrane. In (2.1b), a_c is a constant parameter representing the F-actin concentration at the chemical equilibrium. It differentiates the states of polymerisation and depolymerization. The polymerisation rate is given by k_a and D_a is a positive diffusion coefficient for F-actin. On the boundary, we take the flow velocity of the actin network $\beta = \omega_n := \partial \mathbf{u} / \partial t$. Here \mathbf{u} is the displacement of the actin network at any given point in space and is computed as the displacement solution obtained from the force balance equation (2.1a). In the interior of the domain, we assume that $\beta = \partial \mathbf{x} / \partial t := \partial \mathbf{u} / \partial t$ where $\partial \mathbf{x} / \partial t$ is the mesh velocity. Thus we have a Lagrangian description of the domain evolution.

2.1 Initial and boundary conditions

We define the initial domain Ω_0 , $t = 0$, to be a unit disk. We prescribe the initial conditions for actin density a_0 to correspond to random small perturbations around the homogeneous steady state of the cell. This state biologically corresponds to the cell condition right after mitosis (i.e. cell division) with the cell having a perfectly circular shape. We assume that at the initial time, the cell is unstrained from its original position. The boundary conditions in (2.1e) specify a zero flux boundary for the reaction–diffusion equation (2.1b) and a stress free boundary for the force balance equation (2.1a).

Remark 2.1 We note that in a previous work by Stephanou et al. (2004), the displacement $\mathbf{u}(\mathbf{x}(t), t)$ was taken to be the displacement of the elements of the actin network from the original unstrained position. In this work, we compute the displacement $\mathbf{u}(\mathbf{x}(t), t)$ continuously given the previous positions of $\mathbf{x} \in \Omega_t$, at time $t \in I$.

This assumption implies that at each time t , the elastic forces in (2.1a) are negligible and the viscous forces dominate. An advantage of this modification is that the cell is no longer rigid but can translate, expand and contract.

3 Linear stability analysis of the model equations

In this section we carry out linear stability analysis of the mathematical model. But first we non-dimensionalize the system of equations. This reduces the number of parameters making the mathematical analysis afterwards more amenable.

3.1 Nondimensionalization

Let the length scale L be a typical radius of a cell. Substituting the following dimensionless quantities into (2.1a) and (2.1b),

$$\begin{cases} \tilde{t} = tk_a, & \tilde{a} = \frac{a}{a_c}, & \tilde{\mathbf{u}} = \frac{\mathbf{u}}{L}, & \tilde{\nabla} = L\nabla, & \tilde{\Delta} = L^2\Delta, & \tilde{a}_{sat} = \frac{a_{sat}}{a_c}, \\ \tilde{p} = p \frac{1+\nu}{E}, & \tilde{\phi} = \phi, & \tilde{\epsilon} = \epsilon, & \tilde{\mu}_i = \mu_i k_a \frac{1+\nu}{E}, & \tilde{\psi} = \psi a_c^2 \frac{1+\nu}{E}, \\ \tilde{\beta} = \frac{\beta}{k_a L}, & d = \tilde{D}_a = \frac{D_a}{k_a L^2}, \end{cases} \quad (3.1)$$

results in

$$\begin{cases} \nabla \cdot \{(\mu_1 \epsilon_t + \mu_2 \phi_t \mathbf{I}) + (\epsilon + \nu' \phi \mathbf{I}) + \psi a^2 e^{-a/a_{sat}} \mathbf{I}\} \\ + \nabla \cdot \left\{ \frac{p}{1+\phi} \left[1 + \frac{2}{\pi} \delta(l) \arctan(a) \right] \mathbf{I} \right\} = 0, \\ \frac{\partial a}{\partial t} - d \Delta a + \nabla \cdot (a \beta) = 1 - a, \end{cases} \quad (3.2)$$

where $\nu' = \frac{\nu}{1-2\nu}$, $\nu \neq 0.5$. In the above, we have dropped the tildes without any loss of generality.

3.2 Parameter values

We assign numerical values to all the dimensional model parameters except p and ψ . We note that we do not assign values to the pressure coefficient p and the contractile coefficient ψ yet because we desire to choose their values such that the dispersion relation will have a finite number of unstable modes. The dimensional parameter values are displayed in Table 1.

Some of the parameter values are close to those available in the literature. In Stephanou et al. (2004), a diffusion coefficient D_a in the range $0.00962 - 0.134 \text{ cm}^2/\text{s}$ and an actin saturation concentration a_{sat} of 1.1 normalised density were used. Viscosity of Fibroblast cells is given in Bausch et al. (1998) to be 200 dyn/cm^2 . Here

Table 1 Dimensional parameters and their values as used in the mathematical model except where it is specified otherwise

Parameter	Meaning	Value	Ref.
E	Young's modulus of the actin network	1.5 dyn/cm^2	Estimated
ν	Poisson's ratio of the actin network	0.3	Estimated
D_a	Diffusion coefficient of actin	$0.012 \text{ cm}^2/\text{s}$	Stephanou et al. (2004)
k_a	Polymerisation rate of the actin network	0.03 s^{-1}	Estimated
a_{sat}	Saturation concentration of F-actin	1.4 normalised density	Stephanou et al. (2004)
μ_1	Shear viscosity of the actin network	96.15 dyn s/cm^2	Bausch et al. (1998)
μ_2	Bulk viscosity of the actin network	250 dyn s/cm^2	Bausch et al. (1998)
l_0	Specifies the vicinity of the membrane	80% of the cell radius	Estimated
a_c	F-actin concentration at the chemical equilibrium	1.0 normalised density	Derived from model

Table 2 Non-dimensional parameters and their values as used in the nondimensionalized mathematical model except where it is specified otherwise

Parameter	Meaning	Non-dimensional value
d	Diffusion coefficient of actin	0.4
a_{sat}	Saturation concentration of F-actin	1.4
μ_1	Shear viscosity of the actin network	2.5
μ_2	Bulk viscosity of the actin network	6.5
ψ	Contractility coefficient of the actin network	62.4
p	Pressure coefficient of the actin network	0.26
l_0	Specifies the vicinity of the membrane	0.8

These parameter values were obtained from their dimensional counterpart by using (3.1)

we choose the value of the shear viscosity to be 96.15 dyn s cm^2 and the value of the bulk viscosity of the actin network $\mu_2 = 250 \text{ dyn s/cm}^2$ to be larger than that of the shear modulus. This is because F-actin are more resistant to compression than shear (Barnhart et al. 2011).

Using (3.1), we obtain their corresponding non-dimensional parameter values as displayed in Table 2. These non-dimensional parameter values will be helpful in the isolation and study of the dynamics of any isolated wavenumber $k^2 > 0$. Subsequently we will compare solutions predicted by linear stability theory with those obtained from numerical simulations.

3.3 Linear stability analysis on a unit disc

We restrict linear stability analysis to be carried out on a static unit disk. The assumption is that for time $t = t_0 + n\Delta t$, $t > t_0$ with n small, the deformed cell domain is

still very close to a unit disk. Hence linear analysis is valid on Ω_t provided $t \ll 1$ and $\Omega_t \approx \Omega_0$. Here Δt is a small time step.

The steady state solution of (3.2) is $a_s = 1$, $\mathbf{u}_s = 0$. We linearize the system of equations (3.2) by considering the stability of the steady state to small perturbations $a = a_s + \hat{a}$, and $\mathbf{u} = \mathbf{u}_s + \hat{\mathbf{u}}$, where \hat{a} and $\hat{\mathbf{u}}$ are small variations from the steady state. Substituting these into the nonlinear system (3.2) and neglecting all but the linear terms results in the following linear system of partial differential equations:

$$\begin{cases} \nabla \cdot [(\mu_1 \epsilon_t + \mu_2 \phi_t \mathbf{I}) + (\epsilon + v' \phi \mathbf{I}) + \sigma'(1)a \mathbf{I} + p(1 - \phi) \mathbf{I} + p \frac{2}{\pi} \delta(l)a \mathbf{I}] = 0, \\ \frac{\partial a}{\partial t} - d \Delta a + \nabla \cdot (\boldsymbol{\beta}) + a = 0, \end{cases} \quad (3.3)$$

where $\sigma'(1) = \frac{\partial \sigma(a)}{\partial a}|_{a=a_s}$. In the above equation, we have dropped the hats for the sake of notational convenience. We now look for solutions to these linearized equations in the form of

$$a(\mathbf{x}, t) = a^* \exp(\lambda t + i \mathbf{k} \cdot \mathbf{x}) \quad \text{and} \quad \mathbf{u}(\mathbf{x}, t) = \mathbf{u}^* \exp(\lambda t + i \mathbf{k} \cdot \mathbf{x}), \quad (3.4)$$

where λ and \mathbf{k} are respectively the growth rate (also known as an eigenvalue) and the wave vector and a^* and \mathbf{u}^* are constant. If we substitute (3.4) into the linearized system (3.3) and require the solution to be non-trivial, we obtain that (see for example [Lewis and Murray 1991](#)),

$$\begin{vmatrix} \lambda + dk^2 + 1 & \lambda ik \\ -ik\sigma'(1) - ikp \frac{2}{\pi} \delta(l) & \mu k^2 \lambda + k^2(1 + v') - pk^2 \end{vmatrix} = 0, \quad (3.5)$$

where $\mu = \mu_1 + \mu_2$ and $k = |\mathbf{k}|$. The eigenvalues, λ are solutions of the polynomial in λ given by the determinant of the matrix in (3.5) and is given by

$$k^2[\mu \lambda^2 + b(k^2)\lambda + c(k^2)] = 0, \quad (3.6)$$

where $b(k^2) = \mu dk^2 + [1 + v' + \mu - \sigma'(1) - p - \frac{2}{\pi} p \delta(l)]$,

and $c(k^2) = d[1 + v' - p]k^2 + [1 + v' - p]$.

Solving (3.6) results in the dispersion relation

$$\lambda(k^2) = \frac{-b(k^2) \pm \sqrt{b^2(k^2) - 4\mu k^2 c(k^2)}}{2\mu k^2}. \quad (3.7)$$

From the polynomial expression given in (3.6), it is obvious that the dispersion relation is indeterminate when $k^2 = 0$. Thus in the linear stability analysis we shall only consider $k^2 > 0$. Instability will occur for some wavenumber $k^2 > 0$ if the corresponding $\lambda(k^2)$ has $Re(\lambda) > 0$. Below we use Routh–Hurwitz stability criterion ([Edelstein-Keshet 2005](#)) to determine a sufficient condition on the coefficients of the polynomial

Table 3 Possibilities of stable and unstable modes to exist

Possible conditions ($k^2 \neq 0$)	Types of mode	Sign of $\text{Re}(\lambda)$
$b(k^2) > 0$ and $c(k^2) > 0$	Stable modes for all $k^2 > 0$	Negative
$b(k^2) > 0$ and $c(k^2) < 0$	Unstable modes will exist	Positive
$b(k^2) < 0$ and $c(k^2) > 0$	Unstable modes will exist	Positive
$b(k^2) < 0$ and $c(k^2) < 0$	Unstable modes will exist	Positive

(3.6) that would result in $\text{Re } \lambda(k^2) > 0$ for some $k^2 > 0$. A solution with $\text{Re } \lambda(k^2) > 0$ for some $k^2 > 0$ can exist if $b(k^2) < 0$ or $c(k^2) < 0$ or both (see Table 3).

Observe that $c(k^2)$ can either be positive or negative for all values of $k^2 > 0$ depending on the value of p . In particular, if $p > 1 + v'$ then $c(k^2)$ is negative for all values of $k^2 > 0$. $b(k^2)$ can take positive or negative values for some or all of $k^2 > 0$ and this depends on how small or large p and $\sigma'(1)$ are when compared with the other parameters in $b(k^2)$. Therefore instability can occur for some $k^2 > 0$ if one of the following conditions is satisfied:

1. $b(k^2) > 0$ and $c(k^2) < 0$ or
2. $b(k^2) < 0$ and $c(k^2) > 0$ or
3. $b(k^2) < 0$ and $c(k^2) < 0$ (see Table 3 for more detail).

Condition 1 and 3 above will have $c(k^2) < 0$ for all $k^2 > 0$. And the dispersion relation will have an infinite range of unstable modes. Condition 2 can have a dispersion relation with a finite range of unstable modes and shall be used in carrying out the linear stability analysis. We now analyse $b(k^2) < 0$ in detail. We have that

$$b(k^2) = \mu dk^2 + [1 + v' + \mu - \sigma'(1) - p - \frac{2}{\pi} p \delta(l)] := \mu dk^2 + G < 0, \quad (3.8)$$

where $G := [1 + v' + \mu - \sigma'(1) - p - \frac{2}{\pi} p \delta(l)]$. Observe that $b(k^2)$ is less than zero for some k^2 if G takes negative values and $\mu dk^2 < |G|$. Sufficient conditions for $b(k^2)$ to take negative values for some $k^2 > 0$ are:

- (a) $G = 1 + v' + \mu - \sigma'(1) - p - \frac{2}{\pi} p \delta(l) < 0$,
- (b) $\mu dk^2 < |G| = |1 + v' + \mu - \sigma'(1) - p - \frac{2}{\pi} p \delta(l)|$,
- (c) $k_{crit}^2 \geq k_1^2$,

where $k_{crit}^2 = |G|/\mu d$ is the value of k^2 for which $b(k^2)$ is zero and k_1^2 is the first positive wavenumber. The last condition enforces that $b(k^2)$ is negative for at least the first wavenumber, k_1^2 . From conditions 1 and 2 above, we require p or $\sigma'(1)$ to be sufficiently large in order for $b(k^2) < 0$ to exist for some $k^2 > 0$, where

$$\sigma'(1) := \left. \frac{\partial \sigma(a)}{\partial a} \right|_{a=1} = \psi \left[-\frac{1}{a_{sat}} e^{-\frac{1}{a_{sat}}} + 2e^{-\frac{1}{a_{sat}}} \right]. \quad (3.9)$$

From (3.9), we see that $\sigma'(1)$ is dependent on a_{sat} and also proportional to ψ (see Fig. 3). In particular, if $a_{sat} = 0.5$ then $\sigma'(1) = 0$ and if $0 < a_{sat} < 0.5$ then

Fig. 3 A plot of $\sigma'(1)$ against a_{sat} with $\psi = 1.0$

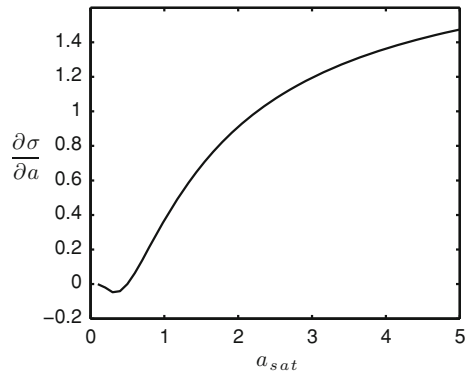


Table 4 A display of the values of $\tilde{\psi}$ (and their corresponding dimensional values of ψ) required by the dispersion relation in order to isolate at least two unstable wavenumbers

Value of $\tilde{\psi}$	Value of ψ (dyn/cm ²)	Wavenumbers isolated (i.e unstable)
62.439	72.045	$k_{0,1}^2, k_{1,1}^2$
95.327	109.993	$k_{0,1}^2, k_{1,1}^2, k_{2,1}^2$
131.869	152.157	$k_{0,1}^2, k_{1,1}^2, k_{2,1}^2, k_{0,2}^2$
174.767	201.654	$k_{0,1}^2, k_{1,1}^2, k_{2,1}^2, k_{0,2}^2, k_{3,1}^2, k_{4,1}^2$
270.094	311.647	$k_{0,1}^2, k_{1,1}^2, k_{2,1}^2, k_{0,2}^2, k_{3,1}^2, k_{4,1}^2, k_{1,2}^2, k_{5,1}^2$
317.758	366.643	$k_{0,1}^2, k_{1,1}^2, k_{2,1}^2, k_{0,2}^2, k_{3,1}^2, k_{4,1}^2, k_{1,2}^2, k_{5,1}^2, k_{2,2}^2$

$\sigma'(1) < 0$. When $\sigma'(1) < 0$ then $b(k^2) < 0$ will exist for some $k^2 > 0$ only if p is sufficiently large such that the three sufficient conditions for $b(k^2) < 0$ are satisfied. Since zero-flux boundary conditions are specified on the boundary $\partial\Omega_t$, we assume that saturation concentration $2a_{sat} > a_s = 1.0$ where a_s is the concentration of actin at the steady state. We carry out a detailed analysis of the dispersion relation by considering the possibility of $b(k^2) < 0$ and $c(k^2) > 0$ for some $k^2 > 0$ to exist (see Appendix A). The purpose of the linear stability theory are two-fold: (a) to validate the numerical scheme and (b) to identify key bifurcation parameters. We will show later that the numerical results are consistent with predictions from the linear stability theory close to bifurcation points. For brevity sake, we show below the predictions from linear theory and present the analysis in Appendix A.

3.3.1 Predictions from linear theory

The wavenumber k^2 are discrete. In Table 4, we give the values of ψ required by the dispersion relation to isolate a couple of wavenumbers. Also in Figs. 4 and 5 we show possible single and mixed modes that could evolve for bands of wavenumbers given in Table 4.

Fig. 4 A surface plot of the vibration mode $w_{1,1}(r, \theta) = J_1(j'_{1,1}r) \cos \theta$ which corresponds to the lowest non-zero wavenumber $k_{1,1}^2$ on a unit disk

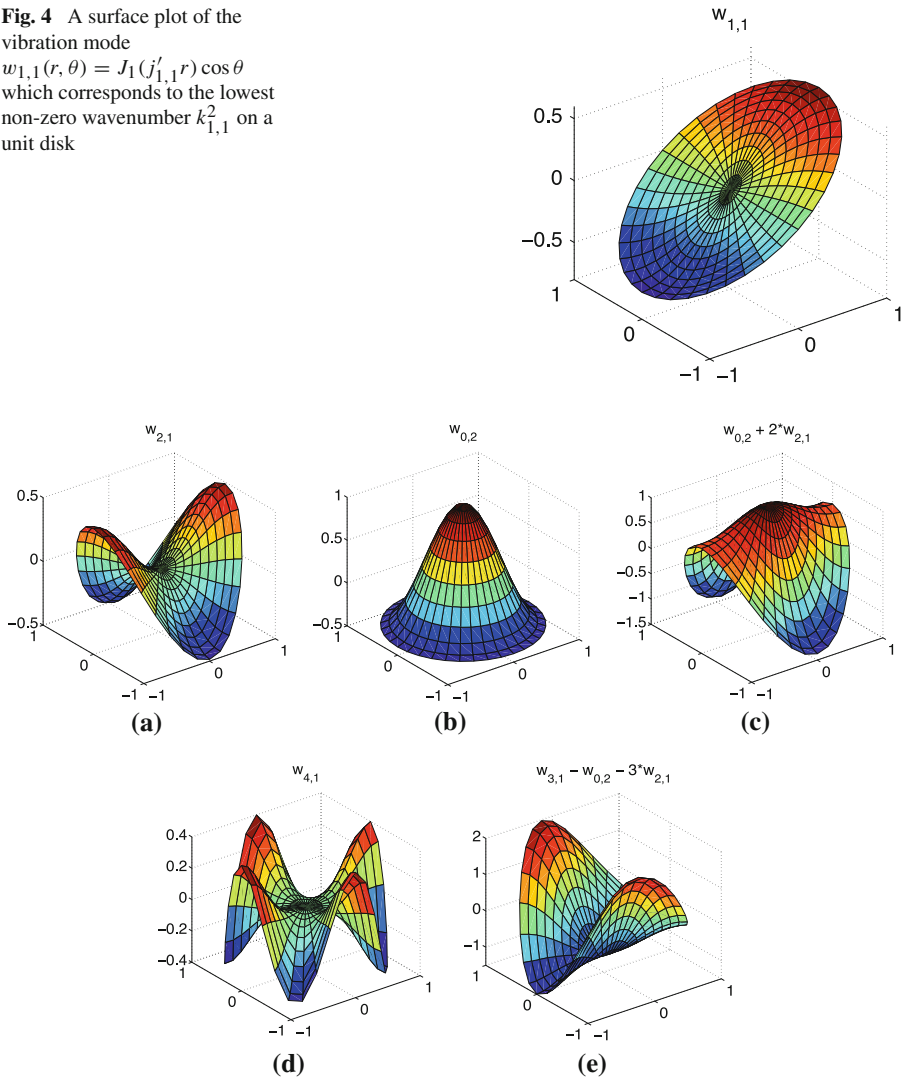


Fig. 5 Surface plots of selected eigenmodes for the bands of wavenumbers displayed in Table 4

4 The moving grid finite element method

To approximate the mathematical model (2.1), we use the finite element method (Strang and Fix 1988; Johnson 1987; Zienkiewicz 1977), a numerical method for computing approximate numerical solutions of partial differential equations (PDE) (Reddy 1993). The method is based on discretizing the domain into a set of finite elements. The discretization process renders the PDE into a system of algebraic equations for the approximate solution which approximates the continuous problem (Sadd 2005).

The moving grid finite element method (Madzvamuse et al. 2003) which we employ here is suitable for moving boundary problems where the domain of the problem is continuously deforming in time. In this method, the nodes of the computational grid are allowed to move. The nodal movement can be determined or prescribed by defining a function that describes the nodal movement (Madzvamuse et al. 2003). Here the velocity of the grids are computed from the displacement solutions of the force balance equation. The methodology of the moving grid finite element method and details of the finite element derivations are given in Appendix B.

5 Numerical results

In this section we present results obtained from the numerical simulations of the finite element scheme. We also validate the numerical results using predictions from linear theory close to bifurcation points. Let $t = n\Delta t$, where Δt and n denotes the time-step size and number of time-steps respectively. The initial domain we consider is a unit disk Ω_0 . We assume that at time $0 < t_s \ll 1$ the domain evolution is negligible and based on this assumption we are able to compare the finite element solutions to predictions from linear stability theory. The perturbations used in the initial conditions will be dependent on the eigenmode we seek to excite. We subsequently show that the finite element scheme gives numerical results that are consistent with those predicted by linear stability theory. In all our simulations rnd denotes a randomly generated number between 10^{-3} and 10^{-5} .

5.1 Validating numerical results using linear stability theory close to bifurcation points

In this section we validate the numerical results by comparing the numerical results to those obtained by using linear stability theory close to bifurcation points.

5.1.1 Excitation of the eigenmode $w_{1,1}$

We present the numerical results for actin concentration \mathbf{a}_h and the displacement solutions \mathbf{u}_h in Fig. 6a and b respectively. These results are consistent with those predicted by linear stability theory as given in Fig. 4. The initial conditions used were $1.0009 + rnd * \sin(x)$, a finite element mesh with 2,113 nodes was used and $\Delta t = 1.0228 \times 10^{-2}$. Numerical results in Fig. 6a and b were obtained after two and four time-steps respectively.

5.1.2 Excitation of the eigenmode: $-w_{0,2}$

Let us fix $\tilde{p} = 1.646$ and $\tilde{\psi} = 38.24$ respectively. For these parameter choices, the dispersion relation again isolates the lowest non-zero wavenumber $k_{1,1}^2$. The initial conditions of the actin concentration are chosen to be equal to $a_c + rnd * \cos(x)$. We found that by choosing the perturbations in the initial conditions to be $rnd * \cos(x)$,

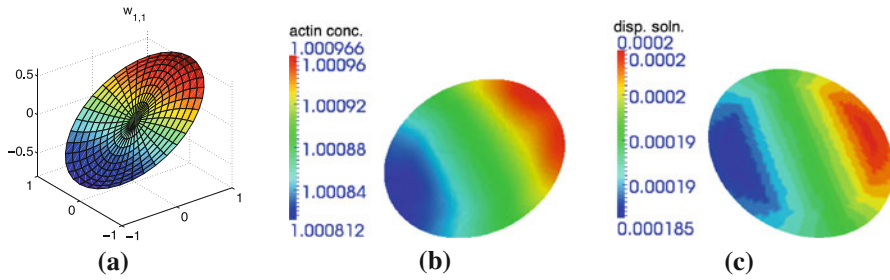


Fig. 6 Surface plots of the numerical results for actin concentration \mathbf{a}_h and displacement solution \mathbf{u}_h . Parameter values used in the numerical simulations are selected such that the lowest non-zero wavenumber $k_{1,1}^2$ is excited. **a** The predicted solution for $w_{1,1}$ from linear theory. **b** The numerical result for actin concentration \mathbf{a}_h while **c** is the numerical result for displacement solution \mathbf{u}_h

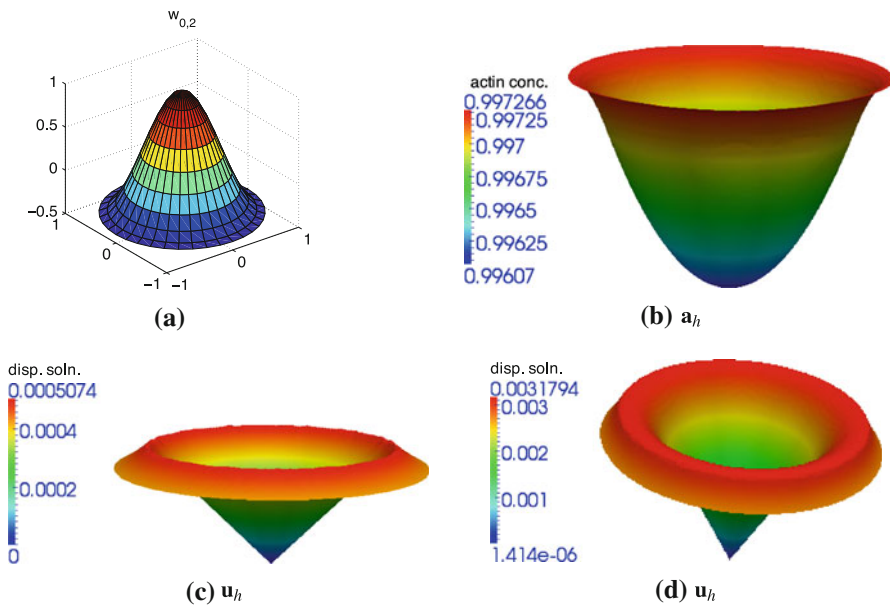


Fig. 7 Surface plots of the numerical results for the actin concentration \mathbf{a}_h and the displacement solution \mathbf{u}_h showing the replication of the eigenmode $-w_{0,2}$. **a** A surface plot of the eigenmode $w_{0,2}$. **b** and **c** Display the simulation results of actin concentration \mathbf{a}_h and displacement solutions \mathbf{u}_h respectively at time $t = 3.61 \times 10^{-3}$. **d** Displays the displacement solutions \mathbf{u}_h at time $t = 0.024$ having no oscillations at the points of discontinuity. The initial conditions used for actin concentrations are $a_c + \text{rnd} * \cos(x)$

we encouraged the excitation of the eigenmode $-w_{0,2}$, where $w_{0,2}$ is the lowest eigenmode. The numerical simulation results are shown in Fig. 7 for the actin concentrations \mathbf{a}_h and the displacement solutions \mathbf{u}_h . For the sake of the comparison of the eigenmode $w_{0,2}$ to the numerical solutions we present in Fig. 7a a plot of the eigenmode $w_{0,2}$.

In Fig. 7c, we observe that the displacement solutions \mathbf{u}_h has its highest value around the points where $x^2 + y^2 = 0.8$. These points correspond to the points where $\delta(l)$ is discontinuous. From the linear analysis in Sect. A.1.2, we know that the dispersion relations is discontinuous at the points where $\delta(l)$ is discontinuous. To

further illustrate the effect of the discontinuity of $\delta(l)$ on the numerical results, we redefine $\delta(l)$ such that $\delta(l) = 1$ on the boundary of the domain and zero elsewhere, i.e.

$$\delta(l) = \begin{cases} 1 & \text{on the cell membrane (i.e the domain boundary),} \\ 0 & \text{elsewhere.} \end{cases} \quad (5.1)$$

We use parameter values that are consistent with those displayed in Table 1. The numerical simulation with $\delta(l)$ defined as in (5.1) gives numerical results where the displacement solution \mathbf{u}_h has its highest value around the boundary.

5.2 Validating numerical results using linear stability theory far from bifurcation points

Far from the bifurcation points of $k_{1,1}^2$, we have the possibility of exciting mixed or higher modes. Below we present the numerical results for actin concentration \mathbf{a}_h and displacement solutions \mathbf{u}_h showing the excitation of mixed and higher modes.

5.2.1 Excitation of mixed and higher modes

The excitation of mixed and higher modes is possible if the value of $\tilde{\psi}$ is allowed to vary while all other parameter values are fixed (see Table 4 for possible values of $\tilde{\psi}$ and the corresponding number of modes the dispersion relation isolates). We present in Figs. 8 and 9 the simulation results for actin concentration \mathbf{a}_h and the displacement solutions showing the excitation of mixed and higher modes respectively. All graphics were saved after no more than 15 time-steps. We present in Table 5 the value of ψ used in the numerical simulations. A comparison of the predicted solutions from linear theory (Fig. 8a and d) with the numerical results (Fig. 8b–c and e–f) show that the numerical scheme reproduces results in close agreement to those predicted by linear stability theory for the mixed and higher modes for the actin concentration. The displacement solutions are naturally small with small amplitudes since they generate the velocity for the domain deformation. Hence we do not expect solution profiles corresponding to the displacement to have high amplitudes compared to the actin concentration profiles.

5.3 Numerical simulations of cell dynamics far away from bifurcation points

From now onwards, we will present the numerical experiments carried out in Sect. 5.1 by considering the long time behaviour far away from the unit disk where linear stability theory no longer holds.

The numerical results show that regions where there is a high actin concentration result in large cell deformations and movement. If the actin concentration is uniformly distributed, then cell deformation and movement is also uniform and isotropic. In all our results, from now onwards, we only present 2D plots corresponding to the actin

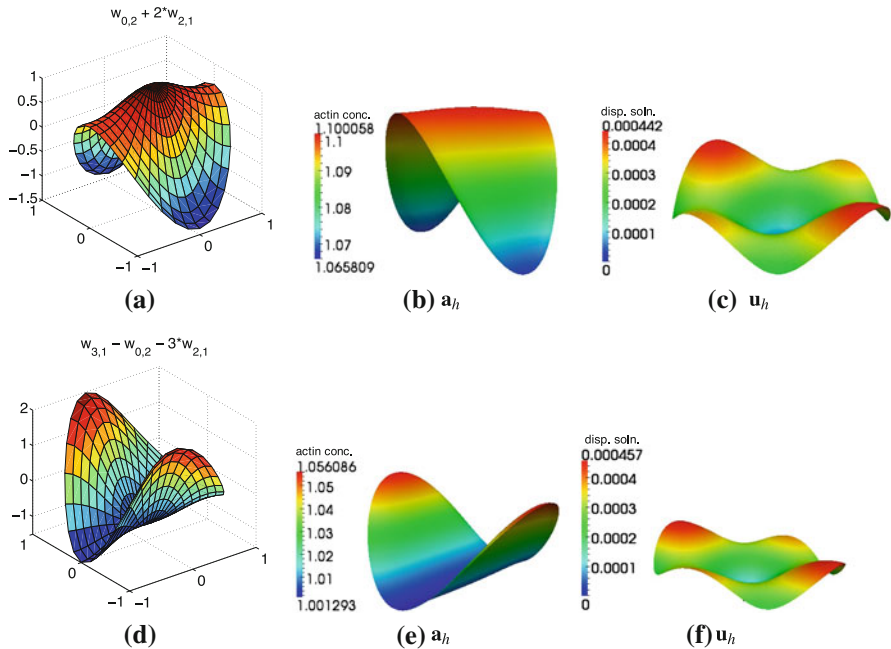


Fig. 8 Surface plots of the numerical results of the actin concentration a_h and displacement solutions u_h having mixed modes excited together with the reproduced solutions predicted from linear theory. **a** and **d** The predicted solutions from linear theory for $w_{0,2} + 2w_{2,1}$ and $w_{3,1} - w_{0,2} - 3w_{2,1}$ respectively. The numerical results reproduce the following modes: **b, c** $w_{0,2} + 2w_{2,1}$, **e, f** $w_{3,1} - w_{0,2} - 3w_{2,1}$. ψ is chosen as given in Table 5 such that mixed modes are excited (refer to the list given in Table 4 for more detail on the eigenmodes isolated by a dispersion relation depending on the value of $\tilde{\psi}$ and ψ)

concentration. The 2D plots corresponding to the displacement are either in (or out of) phase with those of the actin concentration.

5.3.1 Cell evolution for the case where the eigenmode $w_{1,1}$ is excited

In Fig. 10 we present numerical results computed with parameter values selected such that $w_{1,1}$ is excited initially (see Fig. 6). It can be observed that at the early stages ($t = 0.5114$, Fig. 10a) the cell expands uniformly, with actin uniformly distributed around the periphery (boundary) of the cell. Further growth ($t = 1.7183$, Fig. 10b), the cell moves in the positive x -direction and continues to expand. It is clear that where there is a high actin concentration, the cell moves preferentially in that direction. At time ($t = 3.365$, Fig. 10c), the cell has translated and expanded significantly and continues to do so. We present in Fig. 10d a plot of the area of the cell against the number of time-steps demonstrating clearly cell expansion during translation and in Fig. 10e we plot the index of polarity against the number of time steps. The index of polarity is the ratio between the short axis and long axis of the smallest ellipse in which the simulated cell is defined. A black plus sign specifies the position of the cell centroid at time $t = 0$.

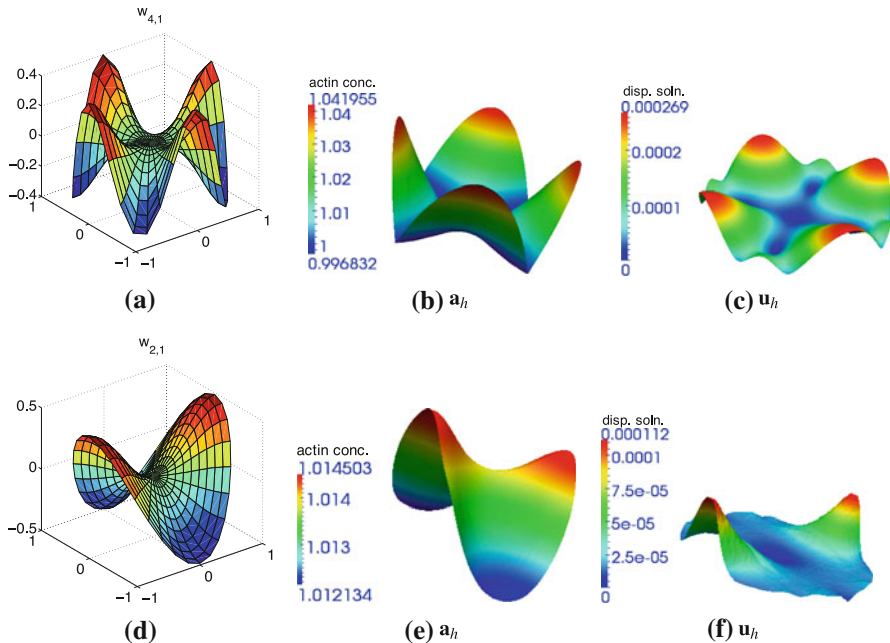


Fig. 9 Surface plots of the numerical results of the actin concentration \mathbf{a}_h and displacement solutions \mathbf{u}_h having higher modes excited together with the reproduced solutions predicted from linear theory. **a** and **d** The predicted solutions from linear theory for $w_{4,1}$ and $w_{2,1}$ respectively. The numerical results reproduce the following modes: **b**, **c** $w_{4,1}$, and **e**, **f** $w_{2,1}$. ψ is chosen as given in Table 5 such that higher modes are excited (refer to the list given in Table 4 for more detail on the eigenmodes isolated by a dispersion relation depending on the value of ψ and ψ)

Table 5 Values of ψ and the initial conditions used for the excitation of mixed and higher modes presented in Fig. 8

Figure	Value of ψ (dyn/cm ²)	Initial conditions for the actin concentration	No. of nodes	Time-step size Δt
Fig. 8b and c	3.1×10^2	$1.0 + 0.1 \cos x $	8, 321	1.0228×10^{-3}
Fig. 8e and f	2.0×10^2	$1.0 + 0.1 \sin^2 y $	8, 321	1.0228×10^{-3}
Fig. 9b and c	3.67×10^2	$1.0 + 0.1 \sin x \sin y $	8, 321	1.0228×10^{-3}
Fig. 9e and f	1.1×10^2	$1.0 + \sum_{i=1}^{20} 0.1 \sin x \sin y $	2, 113	1.0228×10^{-2}

5.3.2 Cell deformation for higher and mixed modes

Here we consider the cell deformation and cell movement for the cases when mixed or higher modes are excited initially.

Cell deformation for the case when the mixed mode $w_{2,1}$ is excited initially

In Fig. 11 we present numerical results with parameter values selected such that $w_{2,1}$ is excited initially. In this plot we observe that as time increases the domain size is

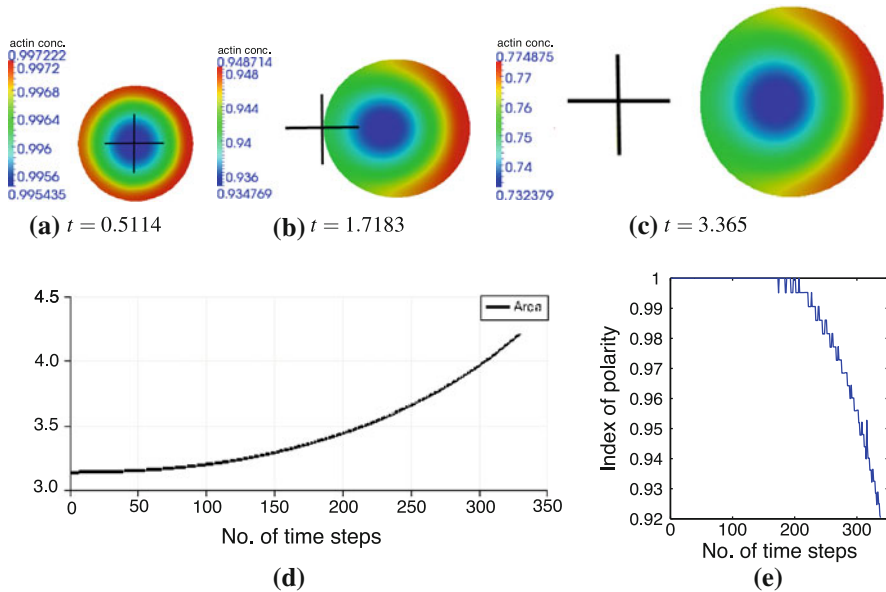


Fig. 10 **a–c** are graphical displays of the numerical results of the actin concentration a_h with $\Delta t = 1.0228 \times 10^{-2}$. *Blue* signifies the lowest values and *red* the highest values. **d** Plot of the area of the cell against the number of time-steps taken. It shows the area of the cell increasing with the number of time-steps taken. **e** Shows a plot of the index of polarity against number of time steps (colour figure online)

increasing and protruding in two fronts but not translating. Actin density is highest at the periphery where protrusions occurs. We present in Fig. 11d a plot of the area of the cell against the number of time-steps. It is clear that the cell is expanding but its centre of origin remains fixed. A plot of the index of polarity against the number of time-step taken is given in Fig. 11e.

*Cell deformation for the case when $w_{3,1} - w_{0,2} - 3 * w_{2,1}$ is excited initially*

The cell deformation for the case when the mixed mode $w_{3,1} - w_{0,2} - 3 * w_{2,1}$ is excited initially is shown in Fig. 12. We observe in this plot that the cell size is increasing along the y -axis and protruding on two fronts. It is not translating and the x -range is decreasing (i.e. in some parts of the domain the cell is contracting inwards). After $n = 130$ time-steps ($t = 0.1329$) actin concentration is still high at the regions where protrusions occur. In general the area of the cell is decreasing. A plot of the index of polarity against the number of time-step taken is shown in Fig. 12d.

*Cell deformation for the case when the mixed mode $w_{0,2} - 2 * w_{2,1}$ is excited*

The cell deformation for the case when the mixed mode $w_{0,2} - 2 * w_{2,1}$ is excited is presented in Fig. 13. In this figure, we observe that the size of the cell is increasing along the y -axis and protruding on two fronts. It is not translating and the x -range is decreasing (i.e. some parts of the cell domain are contracting). Initially actin is high

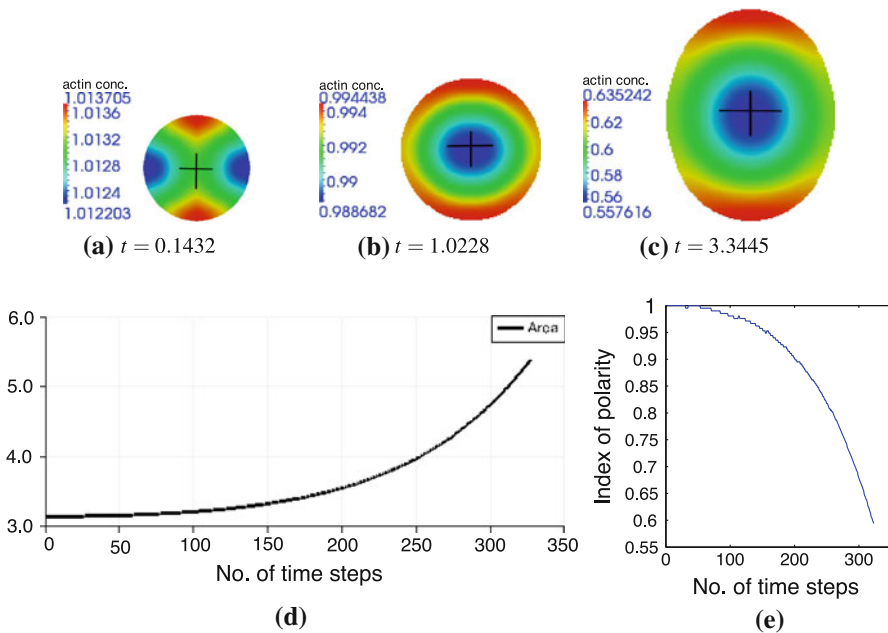


Fig. 11 **a–c** Graphical displays of the numerical results of the actin concentration a_h . A finite element mesh with 2,113 nodes was used, $\Delta t = 1.0228 \times 10^{-2}$. Blue signifies the lowest values and red the highest values. **d** Plot of the area of the cell against the number of time-steps taken. It shows the area of the cell increasing with the number of time-step taken. **e** Plot of the index of polarity against the number of time-step taken (colour figure online)

in the middle region of the cell domain. After $n = 50$ time-steps ($t = 0.0511$) actin concentration is high around the centroid and this is also observed to be the case after $n = 146$ ($t = 1.493$) though the region of highest actin concentration decreases. A plot of the index of polarity against the number of time-step taken is shown in Fig. 13d.

Cell deformation for the case when the mode $w_{4,1}$ is excited

The cell deformation for the case when the mixed mode $w_{4,1}$ is excited is presented in Fig. 14. From Fig. 14 we observe that the cell is increasing in size and actin concentration is highest at regions where protrusion is highest. We present in Fig. 14d a plot of the area of the cell against the number of time-steps illustrating the increase in cell area. The finite element mesh at time $t = 0.1636$ is displayed in Fig. 15.

5.4 Numerical investigation of the dynamics of parameter space $(\tilde{\psi}, \tilde{p})$

On carrying out numerical simulations with parameter values selected from the parameter space $(\tilde{\psi}, \tilde{p})$ close to bifurcation points (see Fig. 23a), we observed that for some choices of $(\tilde{\psi}, \tilde{p})$ in the Hopf region close to the oscillatory region the simulation result gives stationary solutions for actin chemical concentrations that are consistent

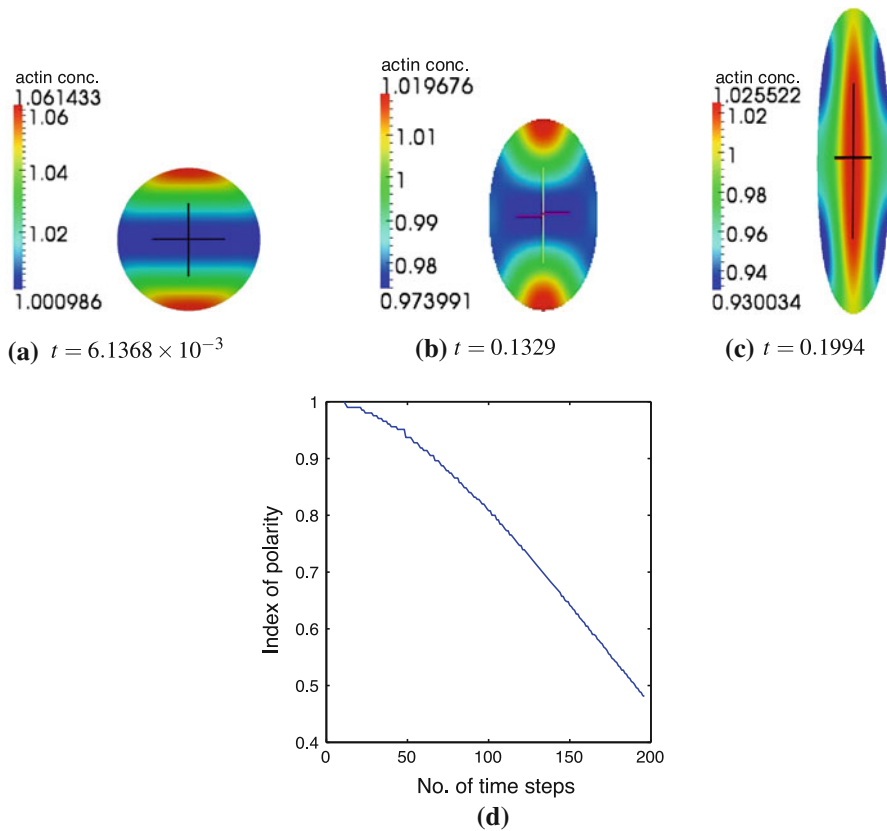


Fig. 12 a–c Graphical displays of the numerical results of the actin concentration a_h . A finite element mesh with 8,321 nodes was used, $\Delta t = 1.0228 \times 10^{-3}$. Blue signifies the lowest values and red the highest values. d Plot of the index of polarity against the number of time-step taken (colour figure online)

with those predicted for the eigenmode $c_1 w_{0,1}$ when the initial conditions used for actin concentrations are $a_c + rnd * \cos(x)$. Fixing $\tilde{\psi} = 38.24$ and decreasing \tilde{p} vertically from 1.75 to 0 we observe that the solutions of the actin concentration reproduce the stationary solutions that are predicted for the eigenmode $c_1 w_{0,1}$ for all values of \tilde{p} considered.

We note that the parameter \tilde{p} can be chosen such that at regions close to the boundary of the domain an oscillatory instability exists and further away from the boundary a Hopf instability occurs. This is possible because of $\delta(l)$ in $b(k^2)$. In such a case where an oscillatory instability exists close to the boundary and further away from the boundary a Hopf instability occurs, numerical simulations give results that are consistent with those predicted for the Turing space from linear theory for the eigenmode $c_1 w_{0,1}$ (results not shown).

We present below the simulation results of parameter spaces with initial conditions for the actin concentrations equal to $a_c + rnd * \cos(x)$ fixed. The observed dynamics of

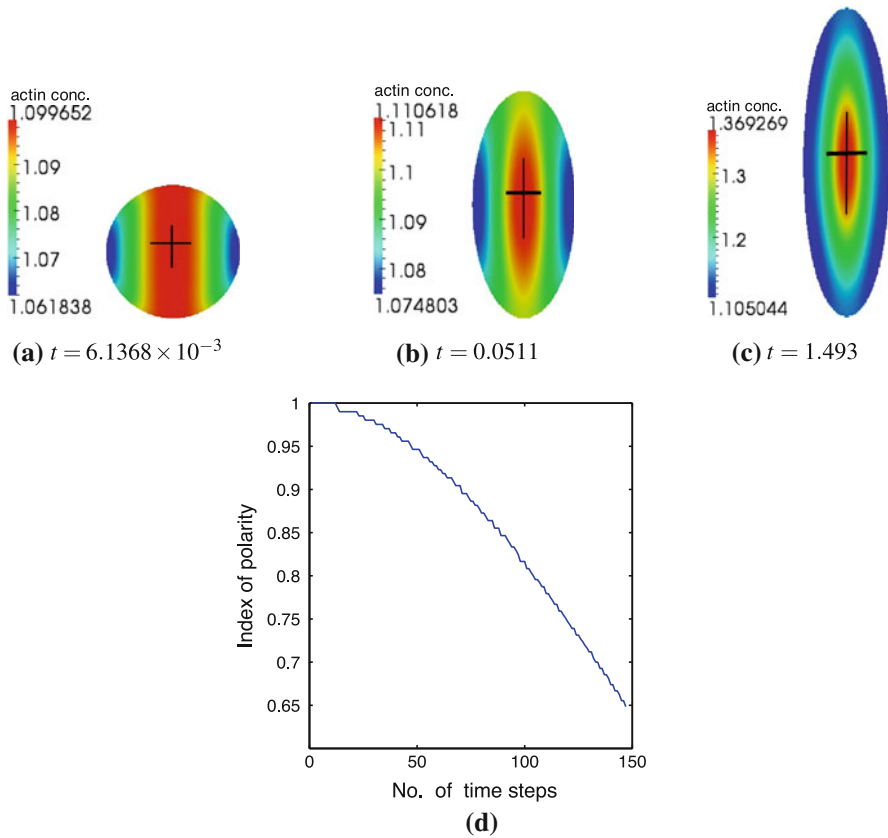


Fig. 13 **a–c** Graphical displays of the numerical results of the actin concentration a_h . A finite element mesh with 8,321 nodes was used, $\Delta t = 1.0228 \times 10^{-3}$. Blue signifies the lowest values and red the highest values. **d** Plot of the index of polarity against the number of time-step taken (colour figure online)

the cell where uniform expansion, uniform contraction and non-uniform deformations of the cell. A finite element mesh with 8,321 nodes was used with $\Delta t = 6.0228 \times 10^{-4}$.

Uniform cell expansion

If we choose the value of the pressure coefficient \tilde{p} to be equal to 3.0 (with all other parameter values staying unchanged as given in Table 2), we observe that the cell deformations correspond to those obtained when $c_1 w_{0,1}$ is excited.

From numerical simulations, we observed that the deformation of the cell is consistent with those obtained when $c_1 w_{0,1}$ is excited, provided $b(k^2)$ isolates only the first non-zero unstable mode $k_{1,1}^2$ and the initial conditions are chosen to be equal to $a_c + \text{rnd} * \cos(x)$.

We also observe that for fixed values of \tilde{p} such that $0 < \tilde{p} < 1.75$ the dynamics of the cell (corresponding to uniform expansions of the cell) is dependent on the value of the contractile tonicity $\tilde{\psi}$ (refer to Fig. 23a for a parameter space plot

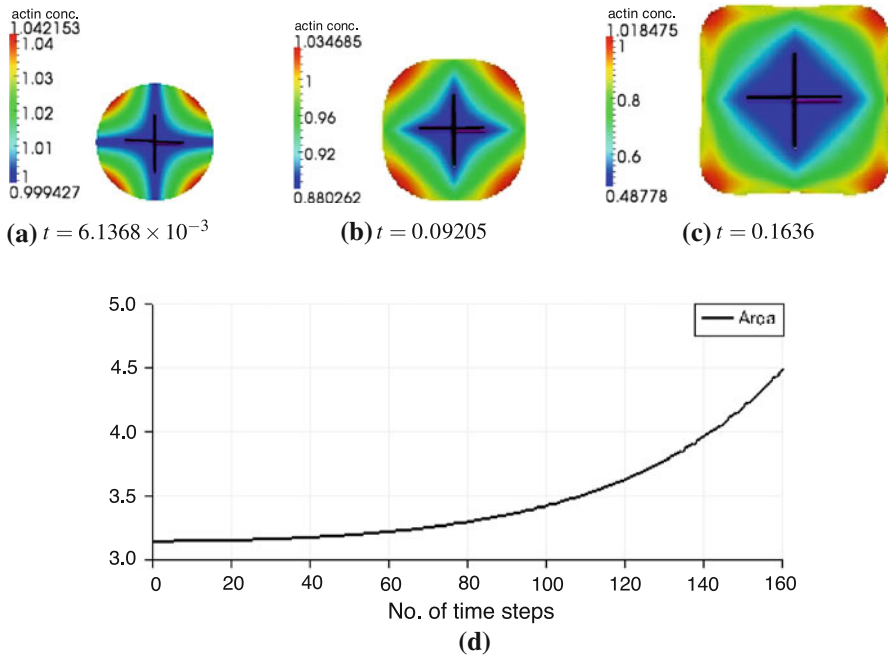


Fig. 14 **a–c** are graphical displays of the numerical results of the actin concentration \mathbf{a}_h with $\Delta t = 1.0228 \times 10^{-3}$. *Blue* signifies the lowest values and *red* the highest values. **d** Plot of the area of the cell against the number of time-steps taken. It shows the area of the cell increasing with the number of time-step taken (colour figure online)

$(\tilde{\psi}, \tilde{p})$). An example is the following: Taking $(\tilde{\psi}, \tilde{p}) = (70.366, 0.026)$ or $(\tilde{\psi}, \tilde{p}) = (70.366, 0.433)$ gives uniform cell expansions while $(\tilde{\psi}, \tilde{p}) = (3.033 \times 10^4, 0.026)$, gives non-uniform cell deformations (results not shown). The simulation results showing the actin concentration solutions with uniform expansions are shown in Fig. 16 for $(\tilde{\psi}, \tilde{p}) = (70.366, 0.433)$. In Fig. 16e we present a plot of the area of the cell against the number of time-steps taken to show the rate at which the area is increasing.

Uniform cell contraction

For the sake of numerical experiment, we allow p to take a negative value. By choosing $\tilde{p} = -0.433$ and $\tilde{\psi} = 70.366$ we observe the cell contracting uniformly at positions that are equidistant from the centroid of the cell domain. And the concentration of actin increases from the boundary to the centroid. We show in Fig. 17 the actin concentration solutions at times (a) $t = 1.2046 \times 10^{-3}$, (b) $t = 3.6137 \times 10^{-3}$, (c) $t = 0.0361$ and (d) $t = 0.5180$. The initial conditions of actin concentration are still equal to $a_c + \text{rnd} * \cos(x)$.

Non-uniform cell deformation

Non-uniform cell deformations occur if all parameter values in Table 2 stay unchanged but $\tilde{\psi}$ is increased or by choosing parameter values $\tilde{\psi}$ and \tilde{p} far away from

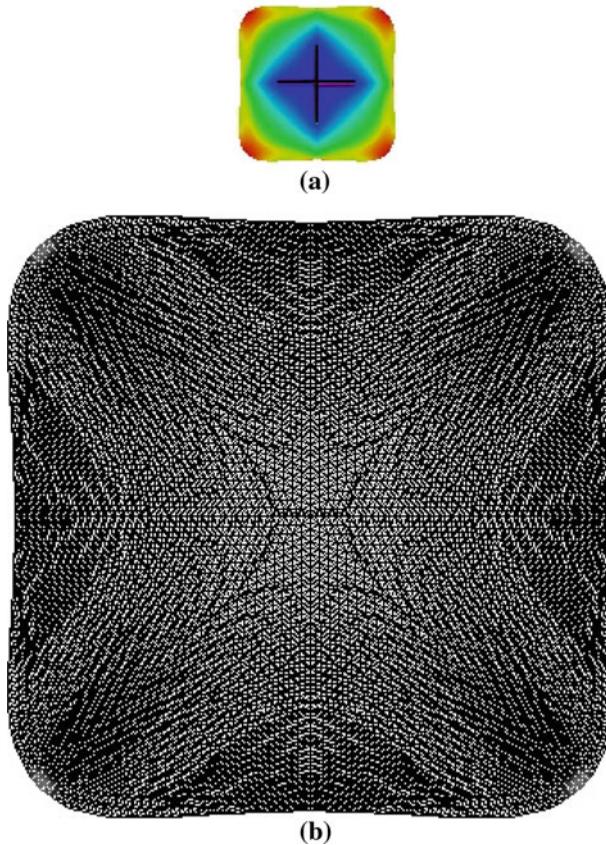


Fig. 15 A graphical display of the finite element mesh. At time $t = 0.1636$, the cell has deformed significantly but the finite element mesh is still suitable for numerical computations and describes the domain properly. **b** The finite element mesh of the graphics given in **a** and has been enlarge for the sake of clarity

bifurcation points [refer to Fig. 23a for a parameter space plot of $(\tilde{\psi}, \tilde{p})$]. Below we give the parameter values and the simulation results for both cases where non-uniform cell deformations occur. Here the initial conditions of actin concentration are given by $a_c + \text{rnd} * \cos(x)$.

- If all model parameter values are kept fixed as given in Table 2, taking increasing values of $\tilde{\psi}$ results in non-uniform cell deformations. For example taking $\tilde{\psi} = 1.04 \times 10^5$, we observed from the numerical results that the cell deforms non-uniformly and rapidly making it impossible to capture the solutions and the numerical algorithm fails.
- If we choose $\tilde{\psi}$ and \tilde{p} arbitrarily such that the parameter space $(\tilde{\psi}, \tilde{p})$ is very far from bifurcation points (for example, $\tilde{\psi} = 7.8 \times 10^3$ and $\tilde{p} = 0.026$), we observe non-uniform cell contraction with actin localised around the centroid of the cell (see Fig. 18). In Fig. 18d we present a plot of the cell area. A plot of the index of polarity against the number of time-step taken is given in Fig. 18e.

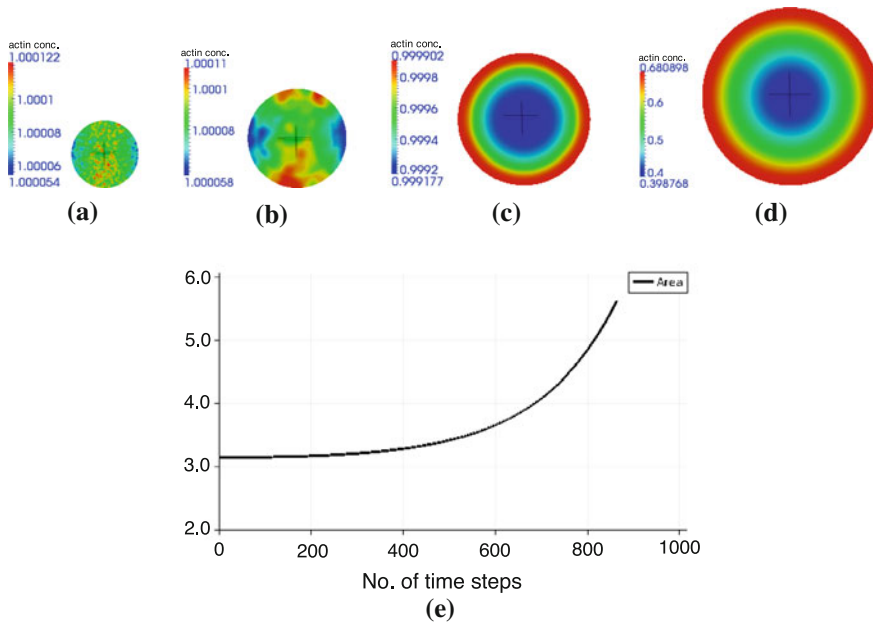


Fig. 16 Graphical display of the simulation results of the actin concentration. Blue denotes the lowest values and red the highest. These results were obtained at the following times: **a** $t = 1.2046 \times 10^{-3}$, **b** $t = 3.6137 \times 10^{-3}$, **c** $t = 0.0361$, and **d** $t = 0.5180$. The numerical value of the contractile tonicity $\tilde{\psi} = 70.366$ and that of the pressure coefficient $\tilde{p} = 0.433$. **e** Plot of the area of the cell against the number of time-steps taken (colour figure online)

- We recall that the simulation results presented in Fig. 18e was obtained for $\tilde{p} = 0.026$ and $\tilde{\psi} = 7.8 \times 10^3$. Now if we decrease only $\tilde{\psi}$ such that $\tilde{\psi} = 1.3 \times 10^3$, we observe cell deformations which agree qualitatively to those observed experimentally (Senju and Miyata 2009). It can be observed that actin concentration is high at the periphery of the cell boundary and is highest at regions where protrusions occur. In Fig. 19, we present the graphical display of the simulation results of the actin concentration. A plot of the index of polarity against the number of time-steps taken is given in Fig. 19g. We can infer from these results that the dynamics of the cell domain, the distribution of actin filaments are related to the pressure coefficient p and the contractile tonicity ψ .

Comparison of Fig. 19f with experimental observations

The distribution of F-actin in cells has been well studied and epifluorescence images are available in the literature. Fig. 20a shows an epifluorescence image of a Swiss 3T3 fibroblast cell obtained from (Senju and Miyata 2009). The fibroblast was stained by the authors for F-actin after being allowed to spread for 1 h. The epifluorescence image shows that F-actin is predominant at the cell periphery and is highest at the regions where protrusions occur. The simulation results presented in Fig. 20b are thus consistent with the experimental observations.

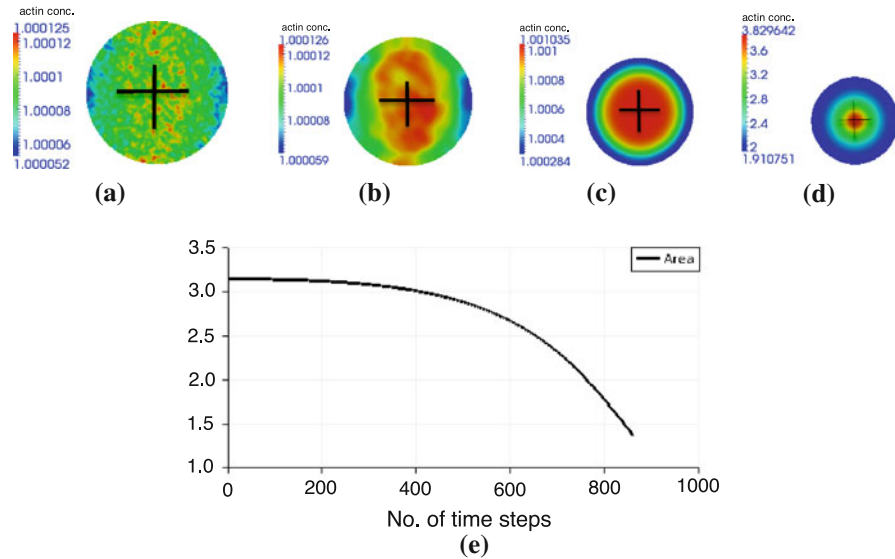


Fig. 17 Graphical display of the simulation results of the actin concentration. Blue denotes the lowest values and red the highest. These results were obtained at the following times: **a** $t = 1.2046 \times 10^{-3}$, **b** $t = 3.6137 \times 10^{-3}$, **c** $t = 0.0361$, and **d** $t = 0.5180$. The numerical value of the contractile tonicity $\tilde{\psi} = 70.366$ and that of the pressure coefficient $\tilde{p} = -0.433$. **e** Plot of the area of the cell against the number of time-steps taken (colour figure online)

Remark 5.1 (Key model parameters) Based on the linear stability analysis and the numerical simulation results we are able to identify key parameters that control cell deformations with respect to the model problem. The contractile tonicity ψ is the bifurcation parameter that determines the transition from stable to unstable state. The actin saturation concentration a_{sat} and the pressure coefficient were also found to play a key role in cell deformations.

6 Numerical simulation on a realistic cell

Here we choose parameters such that they are consistent with those available in the literature such that Young's modulus E of the actin filament is 4000 dyn/cm^2 (Dayel et al. 2009), diffusion coefficient D_a of the actin filament is $1.6 \times 10^{-10} \text{ cm}^2/\text{s}$ (Lanni and Ware 1984; Simon et al. 1988), the polymerization rate k_a is $66/\text{s}$ (Watanabe 2010), the values of the poisson ratio ν , shear and bulk viscosities μ_1 and μ_2 respectively are as given in Table 1. A cell of radius $10 \mu\text{m}$ (0.001 cm) is assumed. We also assume that the pressure coefficient is 800 dyn/cm^2 and the contractile tonicity is $6.9 \times 10^4 \text{ dyn/cm}^2$. We note that for these choice of dimensional parameter values the equivalent non-dimensional parameter values would have a dispersion relation that isolates more than seven wavenumbers inclusive of $k_{4,1}^2$. We used an initial perturbation for actin equal to $|rnd \sin x \sin y|$ in order to bias the excitation of the mode $w_{4,1}$. The numerical simulation result gives protrusion on four fronts and is similar to the result given in Fig. 14.

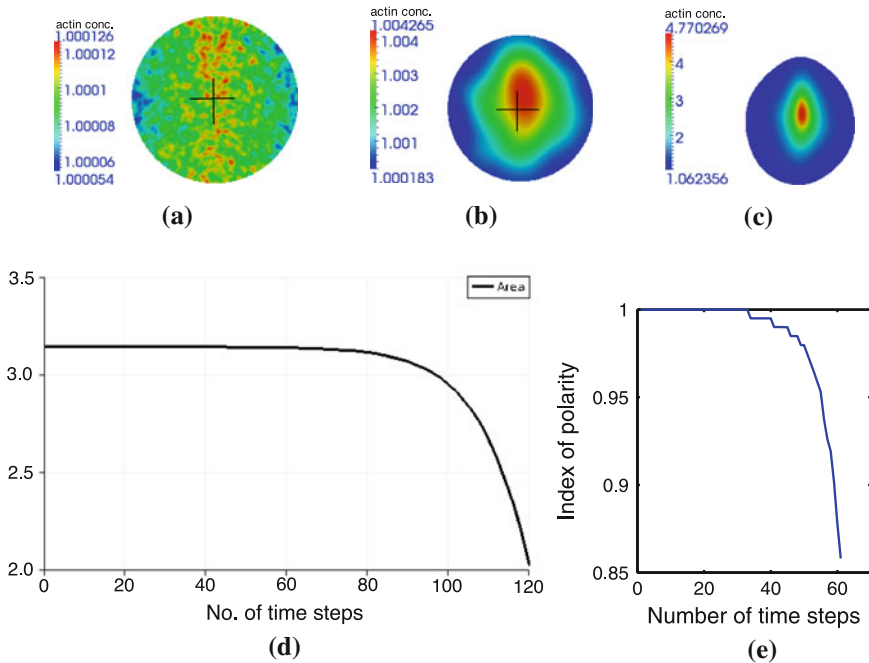


Fig. 18 Graphical display of the simulation results of the actin concentration. *Blue* denotes the lowest values and *red* the highest. These results were obtained at the following times: **a** $t = 1.2046 \times 10^{-3}$, **b** $t = 3.6137 \times 10^{-3}$, and **c** $t = 0.0722$. The numerical value of the contractile tonicity $\tilde{\psi} = 7.8 \times 10^3$ and that of the pressure coefficient $\tilde{p} = 0.026$. **d** Plot of the area of the cell against the number of time-steps taken. **e** Plot of the index of polarity against the number of time-steps for simulation results with contractile tonicity $\tilde{\psi} = 7.8 \times 10^3$ and the pressure coefficient $\tilde{p} = 0.026$ (colour figure online)

7 Conclusion and future work

This article presented detailed analytical and numerical studies of a mathematical model describing cell deformation and cell movement. By taking into account both the biochemical and biomechanical properties of the actin dynamics and filaments resulted in a system of two partial differential equations: the first equation is a force balance equation describing the displacement of the cell generated by the actin filaments and the second, a reaction–diffusion equation describing actin dynamics (Stephanou et al. 2004).

In order to understand the behaviour of the system close to bifurcation points, a detailed linear stability analytical theory was carried out. This enabled us to reduce the number of parameter values within the system but more importantly, we were able to identify two critical parameters underpinning the bifurcation process: the contractile tonicity and the pressure. The contractile tonicity was identified as the bifurcation parameter that determines the transition from a stable homogeneous steady state to non-uniform inhomogeneous solutions. Far away from the bifurcation points, linear theory does not hold, thereby necessitating the use of novel numerical methods.

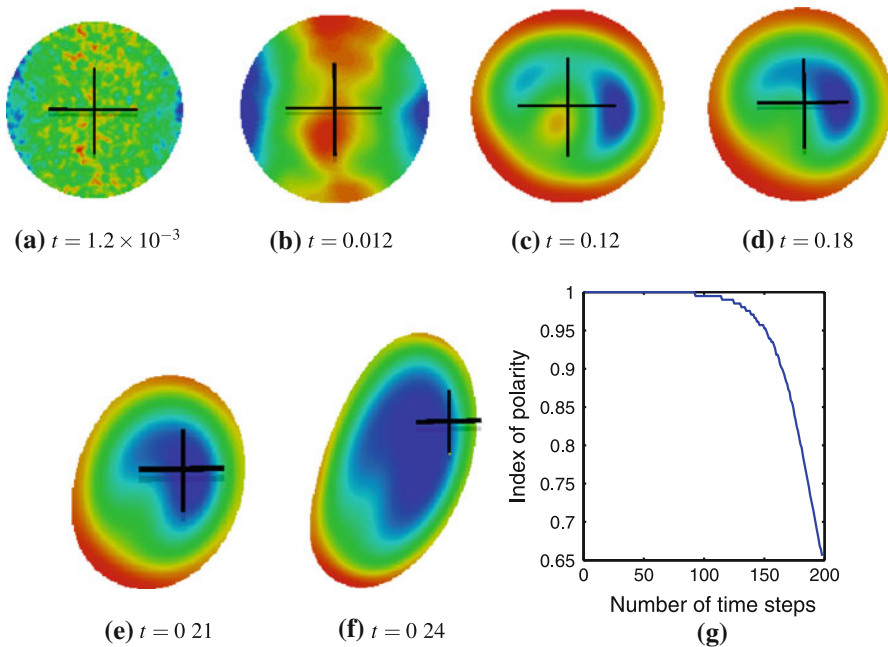


Fig. 19 Graphical display of the simulation results of the actin concentration. *Blue* denotes the lowest values and *red* the highest. The numerical value of the contractile tonicity $\tilde{\psi} = 1.3 \times 10^3$ and the pressure coefficient $\tilde{p} = 0.026$. **g** Plot of the index of polarity against the number of time-steps for simulation results with contractile tonicity $\tilde{\psi} = 1.3 \times 10^3$ and the pressure coefficient $\tilde{p} = 0.026$ (colour figure online)

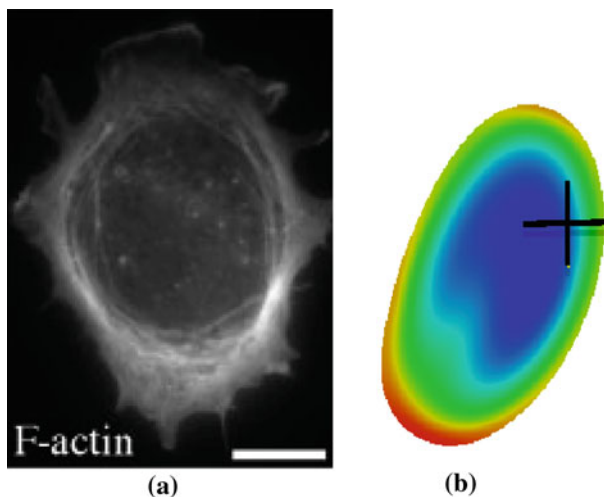


Fig. 20 **a** Epifluorescence image of a Swiss 3T3 fibroblast cell (Senju and Miyata 2009). F-actin is predominant at the cell periphery and is highest at the region where protrusions occur. **b** A simulated cell deformation for contractile tonicity $\tilde{\psi} = 1.3 \times 10^3$ and the pressure coefficient $\tilde{p} = 0.026$. The distribution of F-actin in the simulated cell is in qualitative agreement with experimental observations. Reproduced with permission from Senju and Miyata (2009), Oxford University Press

Unlike other previous studies (Stephanou et al. 2004; Alt and Tranquillo 1995), we proposed a moving grid finite element method introduced in 2000 by (Madzvamuse 2000) to study partial differential equations posed on complex evolving domains. This numerical method is a natural candidate capable, not only of solving the model system, but also of dealing with complex cell shape deformation and movement. By using linear stability theory close to bifurcation points we validated our numerical results which gave confidence in the applicability of the choice of the numerical method. Far away from the bifurcation points, numerical solutions of the model system produced a variety of scenarios of the cell deformation and cell movement such as uniform cell expansion and contraction, and non-uniform cell deformations (for example, cell protrusions). The numerical results clearly demonstrate that regions with high actin concentrations result in large cell deformation and cell movement in complete agreement with experimental observations (Senju and Miyata 2009). Equivalently, regions of the cell with large displacements result in high actin concentrations. If the actin concentration is uniformly distributed, then the cell either expands or contracts uniformly and isotropically.

We summarise our observations as follows:

- The distribution of actin filaments is related to the pressure coefficient, p and the contractile tonicity ψ . Depending on the value of p and ψ the simulation results gave rise to uniform expansion, uniform contraction or non-uniform cell deformations.
- For the cases where contractions occur, actin density was highest around the centroid of the cell while for the cases where expansions occur actin density was highest around the cell periphery.
- For the case of non-uniform cell deformations actin density was predominant at the periphery of the cell and was highest at regions with the highest curvature (see Fig. 19). For $\tilde{\psi} = 7.8 \times 10^3$ actin density was localized at the centroid of the cell and the boundary was contracting non-uniformly (see Fig. 18).
- Actin filaments play a key part in cell deformations and such deformations are a function of the contractile tonicity and an adequate counter pressure is required in the cell to prevent it from shrinking as a result of the contractile forces.
- We assumed that the pressure in the cell was due to the contraction of the network creating cytoplasmic flows throughout the cell thus increasing the pressure and was re-enforced by a polymerisation induced pressure at the vicinity of the cell boundary. We modelled this by introducing the heavy-side function which allowed us to study the pressure-induced protrusion and actin filaments polymerization-induced protrusion.

Acknowledgments UG would like to acknowledge financial support from Akwa Ibom State University Technology Nigeria in support of her DPhil studies. AS acknowledges AM and the Department of Mathematics of the University of Sussex for the two successive invitations in 2007 and 2008 during which this project was initiated and discussed. AM would like to acknowledge support from the EPSRC grant: *Mathematical modelling of spatial patterning on evolving surfaces* (EP/H020349/1), the LMS grant (R4P2), the British Council through its *UK-US New Partnership Fund as part of the Strategic Alliances and Partnerships strand of the Prime Minister's Initiative for International Education 2* (PMI2) and the Royal Society Grant: *A Mathematical Model of Cell Membrane Movement and Deformations* (R4N9).

Mathematical appendices

In these appendices we outline the mathematical aspects of the model that are stated in the main body of the paper. In B, we derive the moving grid finite element method for both the force balance (FBE) (2.1a) and the reaction–diffusion equation (RDE) (2.1a).

Appendix A: Linear stability analysis

A.1 Eigenfunctions of the wave equation on a unit disc

A wavenumber k^2 is the solution of the eigenvalue problem $\Delta \mathbf{w} = -k^2 \mathbf{w}$, $\mathbf{w} \neq 0$ with homogeneous Neumann boundary condition, i.e. $\hat{\mathbf{n}} \cdot \nabla \mathbf{w} = 0$, where \mathbf{w} are time-independent eigenfunctions of the linear system of differential equation (3.3). In order to determine the value of k^2 , we use the separation of variables method to solve for an eigenfunction \mathbf{w} , $\mathbf{w} \neq 0$ and a wavenumber k^2 such that the eigenvalue problem is well defined. We present the result in Remark A.1 (George 2011; Zachmanoglou and Thoe 1986).

Remark A.1 Consider a scalar function w such that $\Delta w = k^2 w$, $w \neq 0$, on a disk $\Omega_0 = \{(x, y) : x^2 + y^2 \leq R^2\}$ with homogeneous Neumann boundary condition. Then the discrete eigenvalues are given by

$$k_{m,n}^2 = (j'_{m,n}/R)^2, \quad m = 0, 1, 2, \dots; \quad n = 1, 2, \dots, \quad (\text{A.1})$$

with corresponding eigenfunctions, $w_{m,n}$ given by

$$w_{m,n}(r, \theta) = \begin{cases} J_0(j'_{0,n}r/R) & \text{if } m = 0, \\ J_m(j'_{m,n}r/R) \cos m(\theta - \theta_1) & \text{if } m > 0. \end{cases} \quad n = 1, 2, \dots,$$

for constants c and θ_1 . Here J_m is the m th Bessel function of the first kind and $j'_{m,n}$ is the n th positive zero of J'_m (except for $j'_{0,1} = 0$), where J'_m denotes the derivative of the Bessel function J_m with respect to r .

Values of $j'_{m,n}$ are obtained from the ‘Handbook of Mathematical Functions with Formulas, Graphs, and Mathematical Tables’ by Abramowitz and Stegun (Abramowitz and Stegun 1968). For the sake of completeness, in Table 6, we present some values of $j'_{m,n}$ for $m = 0, \dots, 5$ and $n = 1, \dots, 4$.

We consider the lowest non-zero wavenumber $k_{1,1}^2 := (j'_{1,1}/R)^2$ and its corresponding vibration mode $w_{1,1}(r, \theta) = J_1(j'_{1,1}r/R) \cos \theta$. Using MATLAB, we compute a surface plot of the vibration mode $w_{1,1}$. The plot is shown in Fig. 4. This plot will be useful in the comparison of the linear stability theory with the numerical results. A way of checking the validity of the numerical results is to show that the numerical scheme computes spatially inhomogeneous steady state solutions which coincides with those predicted by linear stability theory close to bifurcation points (Madzvamuse 2000).

Table 6 Zeros of the derivative of Bessel functions of the first kind: $j'_{m,n}$ $m = 0, \dots, 5$; $n = 1, \dots, 4$

n	$j'_{0,n}$	$j'_{1,n}$	$j'_{2,n}$	$j'_{3,n}$	$j'_{4,n}$	$j'_{5,n}$
1	0.00000	1.84118	3.05424	4.20119	5.31755	6.41562
2	3.83170	5.33144	6.70613	8.01524	9.28240	10.51986
3	7.01558	8.53632	9.96947	11.34592	12.68191	13.98719
4	10.17346	11.70600	13.17037	14.58585	15.96411	17.31284

A.1.1 Parameter values for $c(k^2) > 0$ and $b(k^2) < 0$ to exist for a finite number of $k^2 > 0$

Let us denote here the non-dimensional model parameters by a tilde to avoid confusing it with their dimensional counterpart. Here we assign values to \tilde{p} and $\tilde{\psi}$ such that the dispersion relation isolates a finite number of wavenumbers. We begin by noting the following:

- If $c(k^2) > 0$, for some $k^2 > 0$, then the value of the pressure coefficient \tilde{p} should be chosen such that the inequality $\tilde{p} < 1 + \nu'$ is satisfied. If this inequality is satisfied then $c(k^2) > 0$ for all wavenumbers k^2 [see (3.6) of the function $c(k^2)$]. Thus we will have to rely on $b(k^2)$ for the isolation of a finite number of wavenumbers k^2 (this is a result of the Routh–Hurwitz stability criteria that gives a sufficient condition on the coefficients of the polynomial (3.6) that would result in $\text{Re } \lambda(k^2) > 0$ for some $k^2 > 0$).
- We require $b(k^2) < 0$ for some $k^2 > 0$. Recall that earlier in Sect. 3.3 we outlined the sufficient conditions for $b(k^2) < 0$ for some $k^2 > 0$. From these conditions we know that the value of $b(k^2)$ depends primarily on the value of the pressure coefficient \tilde{p} and the measure of the contractile tonicity $\tilde{\psi}$ for fixed values of \tilde{a}_{sat} .

Thus it is logical to use either \tilde{p} or $\tilde{\psi}$ as the bifurcation parameter but we prefer to use $\tilde{\psi}$ as the bifurcation parameter since there is no restriction on its value (note that \tilde{p} has a restriction on its value since it is required that $\tilde{p} < 1 + \nu'$ for $c(k^2)$ to be positive for any $k^2 > 0$).

Isolation of a finite range of unstable wavenumbers

Here we rely on $b(k^2)$ in order to produce a dispersion relation that isolates a finite range of unstable wavenumbers. $b(k^2)$ is a linear function of k^2 . We begin with the study of the dispersion relation that isolates the wavenumber $k_{1,1}^2$ as its only unstable non-zero wavenumber. The wavenumber $k_{1,1}^2$ is isolated by enforcing the following:

- $b(k^2) < 0$ for $k_{1,1}^2$ but greater than zero for all higher wavenumbers.
- $\tilde{p} < 1 + \nu'$ (recall that enforcing this restriction on \tilde{p} gives $c(k^2) > 0$ for all wavenumbers $k^2 > 0$). Given a Poisson's ratio $\nu := 0.3$ then $\nu' = 0.75$. Hence

$$\tilde{p} < 1 + \nu' = 1.75. \quad (\text{A.2})$$

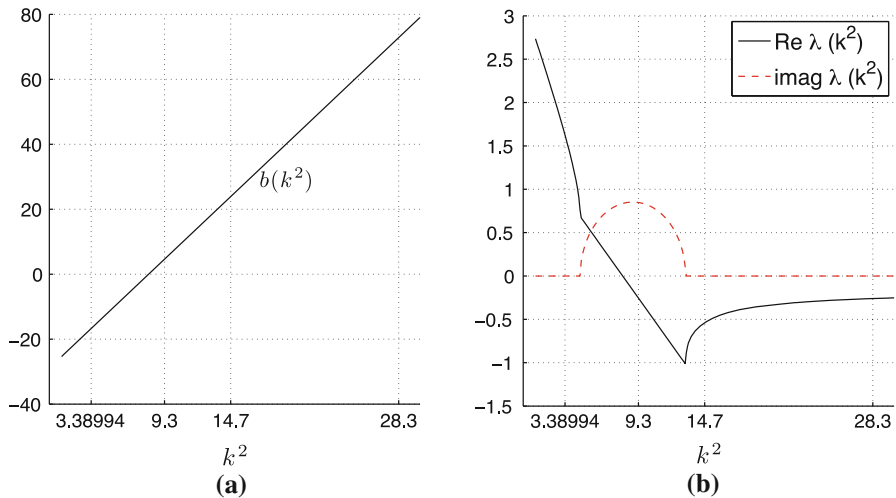


Fig. 21 We present in **a** a plot of $b(k^2) < 0$ when $k_{1,1}^2 = 3.38994$ is the only excitable wavenumber. In **b** we show its corresponding dispersion relation $\text{Re } \lambda$. In both cases $\delta(l) = 1$

Thus to satisfy the inequality (A.2) we assign a value to $\tilde{p} = 0.26$. Next we assign a value to $\tilde{\psi}$ such that the three conditions for $b(k^2) < 0$ as given in Sect. 3.3 are satisfied for only $k_{1,1}^2$. Note that when the value of $\tilde{\psi}$ is gradually increased from $\tilde{\psi} = 0$ we obtain a Hopf bifurcation. If we continue to increase $\tilde{\psi}$ then we get a transition from a Hopf instability to a Turing's instability (see Fig. 23a). A typical value of $\tilde{\psi}$ such that a Turing instability occurs with $k_{1,1}^2$ being the only non-zero wavenumber for which $b(k^2) < 0$ is $\tilde{\psi} = 62.4$ [corresponding dimensional value using the scaling (3.1) is $\psi = 72 \text{ dyn/cm}^2$] irrespective of the value of $\delta(l)$. A plot of $b(k^2)$ and the corresponding dispersion relation $\text{Re } \lambda(k^2)$ against k^2 is shown in Fig. 21 for the case where $\delta(l) = 1$. The plot of $b(k^2)$ and the corresponding dispersion relation $\text{Re } \lambda(k^2)$ against k^2 for the case where $\delta(l) = 0$ is identical to that shown in Fig. 21. We recall that it is not possible to isolate only one non-zero wavenumber except for the case where $k_{1,1}^2$ is isolated. For any wavenumber greater than $k_{1,1}^2$, we only have the choice of isolating the first two non-zero wavenumbers, the first three non-zero wavenumbers, the first four non-zero wavenumbers and so on. For illustrative purposes we present a plot in Fig. 22 of $b(k^2)$ and the corresponding dispersion relation $\text{Re } \lambda(k^2)$ against k^2 where the first two non-zero wavenumbers have been isolated. In validating the numerical results we consider first the case where only $k_{1,1}^2$ is isolated. The advantage of this is that we can easily compare the linear stability theory with the numerical results without having to worry about the dynamics of mixed modes. Next we consider the dynamics of higher modes and mixed modes. To isolate the first two non-zero wavenumbers as shown in Fig. 22, we carried on as we did for $k_{1,1}^2$ but in addition we enforced another condition which is that $k_2^2 < k_c^2 < k_3^2$ irrespective of the value of the heavy-side function $\delta(l)$ in $b(k^2)$, where k_c^2 is the point when $b(k^2) = 0$, $k_2^2 := k_{2,1}^2$ and $k_3^2 := k_{0,1}^2$. See Table 4 for values of $\tilde{\psi}$ and the corresponding band of wavenumbers it isolates (all other model parameter values remain fixed and their values

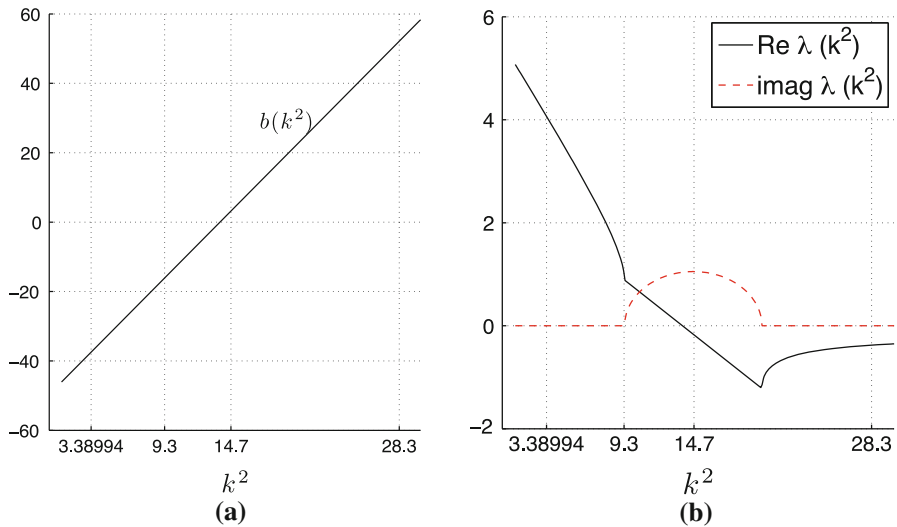


Fig. 22 We present in **a** a plot of $b(k^2) < 0$ when the first two non-zero wavenumbers $k_{1,1}^2 = 3.38994$ and $k_{2,1}^2 = 9.32838$ are the only excitable wavenumbers. In **b** we show the corresponding dispersion relation $\text{Re } \lambda(k^2)$. In both cases $\delta(l) = 1$

are given in Table 2). When a band of wavenumbers is linearly unstable, it is known that it becomes difficult to determine which eigenmode will be excited and in such cases the initial conditions play a key role in determining which eigenmode is excited (Murray 1993). The principle of superposition (Zill and Cullen 2000) implies that any linear combination of eigenmodes is also a solution of the eigenvalue problem. Hence when a band of wavenumbers is isolated by a dispersion relation, it is possible that instead of a single mode being selected a linear combination of eigenmodes (i.e mixed modes) may evolve. In Sect. 5 we present numerical results that show the important role played by the contractile coefficient and the choice of initial conditions on mode selection. For this purpose we present in Fig. 5 surface plots of possible single and mixed modes that could evolve for bands of wavenumbers given in Table 4.

Earlier, we studied the dispersion relation with the value of the pressure coefficient \tilde{p} fixed but the contractility tonicity $\tilde{\psi}$ varied. Various other combinations of $\tilde{\psi}$ and \tilde{p} are possible, hence we study below the parameter space $(\tilde{\psi}, \tilde{p})$.

Parameter space

Here we keep all parameters given in Table 2 fixed except the pressure coefficient \tilde{p} and the contractile tonicity $\tilde{\psi}$. We make a plot of the parameter space $(\tilde{\psi}, \tilde{p})$ showing spaces that lie in a region of Hopf instability ($\text{Re}(\lambda) < 0$ and $\text{Imag}(\lambda) > 0$), oscillatory instability ($\text{Re}(\lambda) > 0$ and $\text{Imag}(\lambda) > 0$) or Turing instability ($\text{Re}(\lambda) > 0$ and $\text{Imag}(\lambda) = 0$) (Moreo et al. 2010; Yang et al. 2002; Cross and Hohenberg 1993). This plot is presented in Fig. 23a for the case where $b(k^2)$ has $\delta(l) = 1$. Note that for $\delta(l) = 0$ the parameter space plot is identical to that shown in Fig. 23a.

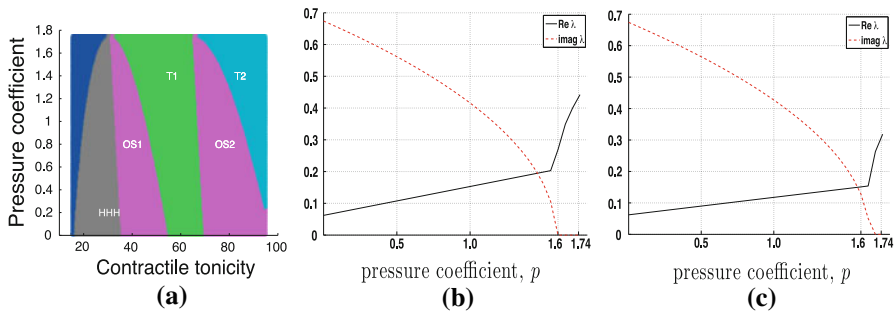


Fig. 23 We present in **a** parameter space plot showing the regions where instability exist for $\delta(l) = 1$. The ash area (H) signifies the region of Hopf instability with a dispersion relation that isolates $k_{1,1}^2$ as the only unstable non-zero wavenumber. The region (dark blue) preceding that of Hopf instability represents the region where the uniform steady state is always stable for all wavenumbers k^2 . Immediately after the Hopf instability region we have a purple region (OS1) where an oscillatory instability exists for $k_{1,1}^2$. The green region is a Turing instability region and has a dispersion relation that isolates $k_{1,1}^2$ as the only unstable non-zero wavenumber. In the purple region (OS2) an oscillatory instability exists for $k_{2,1}^2$. The light blue region is also a Turing instability region and has a dispersion relation that isolates the first two non-zero wavenumbers. And in **b** and **c** we show how the variation of \tilde{p} results in a transition from an oscillatory instability to a Turing instability for $\tilde{\psi} = 38.24$. In **b** $\delta(l) = 1$ and **c** $\delta(l) = 0$ (colour figure online)

In Fig. 23a we observe that there exists Hopf, oscillatory and Turing instability regions where all have a dispersion relation that isolates $k_{1,1}^2$ as the only non-zero wavenumber. The ash area (H) signifies the region of Hopf instability with a dispersion relation that isolates $k_{1,1}^2$ as the only unstable non-zero wavenumber. The region (dark blue) preceding that of Hopf instability represents the region where the uniform steady state is always stable for all wavenumbers k^2 . Immediately after the Hopf instability region we have a purple region (OS1) where an oscillatory instability exists for $k_{1,1}^2$. The green region is a Turing instability region and has a dispersion relation that isolates $k_{1,1}^2$ as the only unstable non-zero wavenumber. In the purple region (OS2) an oscillatory instability exists for $k_{2,1}^2$. The light blue region is also a Turing instability region and has a dispersion relation that isolates the first two non-zero wavenumbers $k_{1,1}^2$ and $k_{2,1}^2$. If we keep $\tilde{\psi}$ constant say $\tilde{\psi} = 38.24$, and then varying \tilde{p} from 0 to 1.74, we observe (from the parameter space plot shown in Fig. 23a for $\delta(l) = 1$) that there exists a transition from an oscillatory to a Turing instability. We make another plot to illustrate better the transition from an oscillatory to a Turing instability for $\tilde{\psi} = 38.24$ by plotting the values of the real and imaginary parts of λ as \tilde{p} varies from 0 to 1.74. This plot is shown in Fig. 23b, c for $\delta(l) = 1$ [i.e. $\sqrt{\xi_x^2 + \xi_y^2} > 0.8$ in the initial domain as defined in (2.6)] and $\delta(l) = 0$ [i.e. $\sqrt{\xi_x^2 + \xi_y^2} < 0.8$ in the initial domain as defined in (2.6)] respectively. Alternatively, if we keep \tilde{p} constant say $\tilde{p} = 0.8$ and then vary $\tilde{\psi}$ from 30 to 60 then we obtain a transition from a stable region to Hopf instability region to an oscillatory instability region and then finally to a Turing instability region for both the case where $\delta(l) = 1$ and $\delta(l) = 0$, $k^2 > 0$ (see Fig. 23a). It is natural to wonder how the solution would behave say in the case where $\tilde{\psi} = 38.24$ and \tilde{p} is varied from 0 to 1.74 such that a transition from an oscillatory instability to a Turing

instability occurs. We studied this numerically by finding the numerical approximation of the model problem (2.1) using the finite element method along with the equivalent numerical value of \tilde{p} which we obtained from the scaling given in (3.1).

Appendix B: Moving grid finite element method

We begin by introducing the following functional spaces and norms.

B.1 Spaces and norms

Let $1 \leq p < \infty$, we define

$$L^p(\Omega_t) = \left\{ v(\mathbf{x}, t) \text{ a measurable function: } \int_{\Omega_t} |v(\mathbf{x}, t)|^p d\Omega_t < \infty \text{ for } \mathbf{x} \in \Omega_t, t \in I \right\}$$

and its corresponding norm

$$\|v(\mathbf{x}, t)\|_{L^p(\Omega_t)} = \left(\int_{\Omega_t} |v(\mathbf{x}, t)|^p d\Omega_t \right)^{\frac{1}{p}}.$$

The set $L^p(\Omega_t)$ is a Banach space. We define the following Hilbert space on $\Omega_t, t \in I$.

$$H^1(\Omega_t) = \left\{ v(\mathbf{x}, t) \in L^2(\Omega_t), D^\alpha v \in L^2(\Omega_t), |\alpha| \leq 1 \right\},$$

for every $t \in I$, where $\alpha = (\alpha_1, \alpha_2)$, $|\alpha| = \alpha_1 + \alpha_2$ and D^α represents the distributional derivative at every time $t \in I$,

$$D^\alpha v = \frac{\partial^{|\alpha|} v}{\partial x^{\alpha_1} \partial y^{\alpha_2}}.$$

B.2 Reynolds transport theorem

Here we state the Reynolds transport theorem. This theorem shall be useful in the derivation of the weak formulation for the RDE.

Theorem B.1 (Reynolds transport theorem) *Let $g(\mathbf{x}, t)$ be a scalar function defined on Ω_t and β be a flow velocity field then*

$$\frac{d}{dt} \int_{\Omega_t} g d\Omega_t = \int_{\Omega_t} \left(\frac{Dg}{Dt} + g \nabla \cdot \beta \right) d\Omega_t \quad (\text{B.1})$$

A proof of this theorem can be found in (Madzvamuse 2000).

B.3 Weak formulation of the model problem

Here we derive the finite element weak formulation of the model problem. Before we begin, we simplify the force balance equation (FBE) by decoupling it into a system of two differential equations; we do this by substituting the values of σ_v , σ_e , σ_c and σ_p as given in (2.3)–(2.5) into the FBE (2.1a) and then decouple the resulting equation. The decoupled system of differential equations of the FBE is thus:

$$\begin{aligned} \frac{\partial}{\partial x} \left(\mathbf{D}_{11} \frac{\partial \dot{u}}{\partial x} + \mathbf{D}_{12} \frac{\partial \dot{v}}{\partial y} \right) + \frac{\partial}{\partial y} \left[\mathbf{D}_{33} \left(\frac{\partial \dot{u}}{\partial y} + \frac{\partial \dot{v}}{\partial x} \right) \right] + \frac{\partial}{\partial x} \left(\mathbf{C}_{11} \frac{\partial u}{\partial x} + \mathbf{C}_{12} \frac{\partial v}{\partial y} \right) \\ + \frac{\partial}{\partial y} \left[\mathbf{C}_{33} \left(\frac{\partial u}{\partial y} + \frac{\partial v}{\partial x} \right) \right] = -\frac{\partial f_1}{\partial x}, \end{aligned} \quad (\text{B.2a})$$

$$\begin{aligned} \frac{\partial}{\partial x} \left[\mathbf{D}_{33} \left(\frac{\partial \dot{u}}{\partial y} + \frac{\partial \dot{v}}{\partial x} \right) \right] + \frac{\partial}{\partial y} \left(\mathbf{D}_{12} \frac{\partial \dot{u}}{\partial x} + \mathbf{D}_{22} \frac{\partial \dot{v}}{\partial y} \right) + \frac{\partial}{\partial y} \left(\mathbf{C}_{12} \frac{\partial u}{\partial x} + \mathbf{C}_{22} \frac{\partial v}{\partial y} \right) \\ + \frac{\partial}{\partial x} \left[\mathbf{C}_{33} \left(\frac{\partial u}{\partial y} + \frac{\partial v}{\partial x} \right) \right] = -\frac{\partial f_2}{\partial y}, \end{aligned} \quad (\text{B.2b})$$

where $f_1 \equiv f_2 = \left[\frac{p}{1+\phi} \left(1 + \frac{2}{\pi} \delta(l) \arctan a \right) + \psi a^2 e^{-a/a_{sat}} \right]$, $\mathbf{D}_{11} = \mathbf{D}_{22} = \mu_1 + \mu_2$, $\mathbf{D}_{12} \equiv \mathbf{D}_{21} = \mu_2$, $\mathbf{D}_{33} = \mu_1/2$, $\mathbf{C}_{11} \equiv \mathbf{C}_{22} = \frac{E(1-\nu)}{(1+\nu)(1-2\nu)}$, $\mathbf{C}_{12} \equiv \mathbf{C}_{21} = \frac{E\nu}{(1+\nu)(1-2\nu)}$ and $\mathbf{C}_{33} = \frac{E}{2(1+\nu)}$.

B.3.1 Weak formulation of the FBE

In order to derive the weak formulation of the force balance equation (FBE), we multiply the system of differential equations for the FBE (B.2) by a test function $w(\mathbf{x}, t) \in H^1(\Omega_t)$, $t \in I$, and using Green's first identity we integrate the differential equation over the domain Ω_t and apply the boundary condition. The weak formulation is thus: Find $u(\mathbf{x}, t)$, $v(\mathbf{x}, t) \in H^1(\Omega_t)$, $t \in I$ such that

$$\begin{aligned} \int_{\Omega_t} \frac{\partial w}{\partial x} \left(\mathbf{D}_{11} \frac{\partial \dot{u}}{\partial x} + \mathbf{D}_{12} \frac{\partial \dot{v}}{\partial y} + \mathbf{C}_{11} \frac{\partial u}{\partial x} + \mathbf{C}_{12} \frac{\partial v}{\partial y} \right) + \frac{\partial w}{\partial y} \left[\mathbf{D}_{33} \left(\frac{\partial \dot{u}}{\partial y} + \frac{\partial \dot{v}}{\partial x} \right) \right] \\ + \frac{\partial w}{\partial y} \left[\mathbf{C}_{33} \left(\frac{\partial u}{\partial y} + \frac{\partial v}{\partial x} \right) \right] d\Omega_t = \int_{\Omega_t} w \frac{\partial f_1}{\partial x} d\Omega_t, \end{aligned} \quad (\text{B.3a})$$

$$\begin{aligned} \int_{\Omega_t} \frac{\partial w}{\partial y} \left(\mathbf{D}_{12} \frac{\partial \dot{u}}{\partial x} + \mathbf{D}_{22} \frac{\partial \dot{v}}{\partial y} + \mathbf{C}_{12} \frac{\partial u}{\partial x} + \mathbf{C}_{22} \frac{\partial v}{\partial y} \right) + \frac{\partial w}{\partial x} \left[\mathbf{D}_{33} \left(\frac{\partial \dot{u}}{\partial y} + \frac{\partial \dot{v}}{\partial x} \right) \right] \\ + \frac{\partial w}{\partial x} \left[\mathbf{C}_{33} \left(\frac{\partial u}{\partial y} + \frac{\partial v}{\partial x} \right) \right] d\Omega_t = \int_{\Omega_t} w \frac{\partial f_2}{\partial y} d\Omega_t, \end{aligned} \quad (\text{B.3b})$$

for all $w(\mathbf{x}, t) \in H^1(\Omega_t)$, $t \in I$. The integrals on the right hand side of the weak formulation (B.3) are difficult to evaluate. To show this we write them out explicitly below.

$$\begin{cases} \int_{\Omega_t} w \frac{\partial f_1}{\partial x} d\Omega_t = \int_{\Omega_t} w \frac{\partial}{\partial x} \left[\frac{p}{1+\phi} \left(1 + \frac{2}{\pi} \delta(l) \arctan a \right) + \psi a^2 e^{-a/a_{sat}} \right] d\Omega_t, \\ \int_{\Omega_t} w \frac{\partial f_2}{\partial y} d\Omega_t = \int_{\Omega_t} w \frac{\partial}{\partial y} \left[\frac{p}{1+\phi} \left(1 + \frac{2}{\pi} \delta(l) \arctan a \right) + \psi a^2 e^{-a/a_{sat}} \right] d\Omega_t, \end{cases} \quad (\text{B.4})$$

since $f_1 \equiv f_2 = \frac{p}{1+\phi} \left(1 + \frac{2}{\pi} \delta(l) \arctan a \right) + \psi a^2 e^{-a/a_{sat}}$. In view of this, we state the following identities which can be derived using the gradient and divergence theorems and are useful in the sequel in rewriting the weak form in a computationally efficient form. Let $r(\mathbf{x}, t)$ and $g(\mathbf{x}, t)$ be scalar functions of class $C^0(\Omega_t)$ defined in $\Omega_t \subset \mathcal{R}^2$ and also let $\hat{\mathbf{n}} = (n_1, n_2)$ denote the outward unit vector normal to $\partial\Omega_t$ for time $t \in I$. Then the following identities holds

$$\begin{cases} \int_{\Omega_t} r \frac{\partial g}{\partial x} d\Omega_t = - \int_{\Omega_t} g \frac{\partial r}{\partial x} d\Omega_t + \int_{\partial\Omega_t} n_1 r g ds, \\ \int_{\Omega_t} r \frac{\partial g}{\partial y} d\Omega_t = - \int_{\Omega_t} g \frac{\partial r}{\partial y} d\Omega_t + \int_{\partial\Omega_t} n_2 r g ds. \end{cases} \quad (\text{B.5})$$

We wish to treat the singularity in (B.4) before applying the identities given in (B.5). This singularity is as a result of the presence of the heavy-side function in the integrand. At the region of discontinuity, the integrand is infinite. We note that the identities given in (B.5) can only be applied to functions of class $C^0(\Omega_t)$. To overcome this we split the integral (B.4) into three integrals at the region of discontinuity (Ambrosio et al. 2000). And we obtain that

$$\begin{cases} \int_{\Omega_t} w \frac{\partial f_1}{\partial x} d\Omega_t = \int_{\Omega_t^0} w \frac{\partial f_1}{\partial x} d\Omega_t + \int_{\Omega_t^1} w \frac{\partial f_1}{\partial x} d\Omega_t + \int_{\Omega_t^{jump}} w \frac{\partial f_1}{\partial x} d\Omega_t, \\ \int_{\Omega_t} w \frac{\partial f_2}{\partial y} d\Omega_t = \int_{\Omega_t^0} w \frac{\partial f_2}{\partial y} d\Omega_t + \int_{\Omega_t^1} w \frac{\partial f_2}{\partial y} d\Omega_t + \int_{\Omega_t^{jump}} w \frac{\partial f_2}{\partial y} d\Omega_t, \end{cases} \quad (\text{B.6})$$

where Ω_t^0, Ω_t^1 are the regions in Ω_t where $\delta(l) = 0$ and 1 respectively. Ω_t^{jump} is the region in $\Omega_t \subset \mathcal{R}^2$ where the discontinuity exist. We note that at the region of discontinuity $\delta(l) = 0$. The integral (B.4) when written in the form (B.6) is continuous and we can apply the identities (B.5) to rewrite the weak form. We note that the weak form shall not be written in the split domain form for the sake of brevity. Using the identities (B.5) we can rewrite the weak form as follows. Find $u(\mathbf{x}, t), v(\mathbf{x}, t) \in H^1(\Omega_t), t \in I$ such that

$$\begin{aligned} \int_{\Omega_t} \frac{\partial w}{\partial x} \left(\mathbf{D}_{11} \frac{\partial u}{\partial x} + \mathbf{D}_{12} \frac{\partial v}{\partial y} + \mathbf{C}_{11} \frac{\partial u}{\partial x} + \mathbf{C}_{12} \frac{\partial v}{\partial y} \right) + \frac{\partial w}{\partial y} \left[\mathbf{D}_{33} \left(\frac{\partial u}{\partial y} + \frac{\partial v}{\partial x} \right) \right] \\ + \frac{\partial w}{\partial y} \left[\mathbf{C}_{33} \left(\frac{\partial u}{\partial y} + \frac{\partial v}{\partial x} \right) \right] d\Omega_t = - \int_{\Omega_t} f_1 \frac{\partial w}{\partial x} d\Omega_t + \int_{\partial\Omega_t} n_1 f_1 w ds, \quad (\text{B.7a}) \end{aligned}$$

$$\int_{\Omega_t} \frac{\partial w}{\partial y} \left(\mathbf{D}_{12} \frac{\partial \dot{u}}{\partial x} + \mathbf{D}_{22} \frac{\partial \dot{v}}{\partial y} + \mathbf{C}_{12} \frac{\partial u}{\partial x} + \mathbf{C}_{22} \frac{\partial v}{\partial y} \right) + \frac{\partial w}{\partial x} \left[\mathbf{D}_{33} \left(\frac{\partial \dot{u}}{\partial y} + \frac{\partial \dot{v}}{\partial x} \right) \right] \\ + \frac{\partial w}{\partial x} \left[\mathbf{C}_{33} \left(\frac{\partial u}{\partial y} + \frac{\partial v}{\partial x} \right) \right] d\Omega_t = - \int_{\Omega_t} f_2 \frac{\partial w}{\partial y} d\Omega_t + \int_{\partial\Omega_t} n_2 f_2 w ds, \quad (\text{B.7b})$$

for all $w(\mathbf{x}, t) \in H^1(\Omega_t)$, $t \in I$. Here n_1 and n_2 are the direction cosines of the outward unit vector, $\hat{\mathbf{n}}$ normal to $\partial\Omega_t$ for time $t \in I$ (i.e. n_1 is the cosine of the angle between the positive x direction and the vector $\hat{\mathbf{n}}$ and n_2 is the cosine of the angle between the positive y direction and the vector $\hat{\mathbf{n}}$). Since the test functions we use are piecewise linear basis functions and their spatial derivatives are easy and straight forward to compute, the weak formulation as expressed in (B.7) is a lot easier to compute compared to (B.3). We say that $u(\mathbf{x}, t)$, $v(\mathbf{x}, t)$ is a weak solution of the FBE (2.1) if $u(\mathbf{x}, t)$, $v(\mathbf{x}, t) \in H^1(\Omega_t)$ and (B.15) holds. Here we have assumed that $a(\mathbf{x}, t)$ is known and is the solution of the reaction–diffusion equation (2.1b).

B.3.2 Weak formulation of the reaction–diffusion equation

Here we recall the reaction–diffusion equation (RDE) for the actin bio-chemical dynamics for completeness and derive a finite element model for this equation. The reaction–diffusion equation for the actin bio-chemical dynamics is:

$$\frac{\partial a}{\partial t} - D_a \Delta a + \nabla \cdot (a\boldsymbol{\beta}) - k_a(a_c - a) = 0. \quad (\text{B.8})$$

By applying the product rule to the transport term in the RDE (B.8), we can rewrite the RDE as follows;

$$\frac{\partial a}{\partial t} - D_a \Delta a + (\nabla a) \cdot \boldsymbol{\beta} + a(\nabla \cdot \boldsymbol{\beta}) - k_a(a_c - a) = 0. \quad (\text{B.9})$$

We would like to represent the partial time derivative in the RDE (B.9) in terms of the material derivative. In view of this, we introduce the material derivative of the actin concentration a . Let Da/Dt be a material derivative, then the material derivative of the actin concentration a is defined as (Reddy 1993);

$$\frac{Da}{Dt} = \frac{\partial a}{\partial t} + (\nabla a) \cdot \boldsymbol{\beta}. \quad (\text{B.10})$$

Upon substituting the material derivative (B.10) into (B.9), we obtain the following differential equation,

$$\frac{Da}{Dt} - D_a \Delta a + a(\nabla \cdot \boldsymbol{\beta}) - k_a(a_c - a) = 0. \quad (\text{B.11})$$

In order to obtain the weak formulation we multiply (B.11) by a test function $w(\mathbf{x}, t) \in H^1(\Omega_t)$, $t \in \mathbf{I}$, and integrate by parts:

$$\int_{\Omega_t} \left[w \frac{Da}{\partial t} + aw(\nabla \cdot \boldsymbol{\beta}) + D_a \nabla a \cdot \nabla w + k_a aw \right] d\Omega_t = \int_{\Omega_t} k_a a_c w d\Omega_t. \quad (\text{B.12})$$

Using the product rule, the differential equation (B.12) can be rewritten as;

$$\begin{aligned} \int_{\Omega_t} \left[\frac{D(aw)}{\partial t} - a \frac{Dw}{\partial t} + aw(\nabla \cdot \boldsymbol{\beta}) + D_a \nabla a \cdot \nabla w \right] d\Omega_t + \int_{\Omega_t} k_a aw d\Omega_t \\ = \int_{\Omega_t} k_a a_c w d\Omega_t. \end{aligned} \quad (\text{B.13})$$

Using the Reynolds transport theorem (see Sect. B.2), we rewrite (B.13) such that the weak formulation reads: Find $a(\mathbf{x}, t) \in H^1(\Omega_t)$, $t \in \mathbf{I}$ such that

$$\begin{aligned} \frac{d}{dt} \int_{\Omega_t} aw d\Omega_t + \int_{\Omega_t} (D_a \nabla a \cdot \nabla w + k_a aw) d\Omega_t = \int_{\Omega_t} k_a a_c w d\Omega_t \\ + \int_{\Omega_t} a \frac{Dw}{Dt} d\Omega_t, \quad \forall w \in H^1(\Omega_t). \end{aligned} \quad (\text{B.14})$$

B.3.3 Weak formulation of the coupled problem

The weak formulation of the coupled problem (2.1) is thus: Find $a(\mathbf{x}, t)$, $u(\mathbf{x}, t)$, $v(\mathbf{x}, t) \in H^1(\Omega_t)$, $t \in I$ such that

$$\begin{aligned} \int_{\Omega_t} \frac{\partial w}{\partial x} \left(\mathbf{D}_{11} \frac{\partial \dot{u}}{\partial x} + \mathbf{D}_{12} \frac{\partial \dot{v}}{\partial y} + \mathbf{C}_{11} \frac{\partial u}{\partial x} + \mathbf{C}_{12} \frac{\partial v}{\partial y} \right) + \frac{\partial w}{\partial y} \left[\mathbf{D}_{33} \left(\frac{\partial \dot{u}}{\partial y} + \frac{\partial \dot{v}}{\partial x} \right) \right] \\ + \frac{\partial w}{\partial y} \left[\mathbf{C}_{33} \left(\frac{\partial u}{\partial y} + \frac{\partial v}{\partial x} \right) \right] d\Omega_t = - \int_{\Omega_t} f_1 \frac{\partial w}{\partial x} d\Omega_t + \int_{\partial\Omega_t} n_1 f_1 w ds, \end{aligned} \quad (\text{B.15a})$$

$$\begin{aligned} \int_{\Omega_t} \frac{\partial w}{\partial y} \left(\mathbf{D}_{12} \frac{\partial \dot{u}}{\partial x} + \mathbf{D}_{22} \frac{\partial \dot{v}}{\partial y} + \mathbf{C}_{12} \frac{\partial u}{\partial x} + \mathbf{C}_{22} \frac{\partial v}{\partial y} \right) + \frac{\partial w}{\partial x} \left[\mathbf{D}_{33} \left(\frac{\partial \dot{u}}{\partial y} + \frac{\partial \dot{v}}{\partial x} \right) \right] \\ + \frac{\partial w}{\partial x} \left[\mathbf{C}_{33} \left(\frac{\partial u}{\partial y} + \frac{\partial v}{\partial x} \right) \right] d\Omega_t = - \int_{\Omega_t} f_2 \frac{\partial w}{\partial y} d\Omega_t + \int_{\partial\Omega_t} n_2 f_2 w ds, \end{aligned} \quad (\text{B.15b})$$

$$\frac{d}{dt} \int_{\Omega_t} a w \, d\Omega_t + \int_{\Omega_t} (D_a \nabla a \cdot \nabla w + k_a a w) \, d\Omega_t = \int_{\Omega_t} k_a a_c w \, d\Omega_t + \int_{\Omega_t} a \frac{Dw}{Dt} \, d\Omega_t, \quad (\text{B.15c})$$

for all $w(\mathbf{x}, t) \in H^1(\Omega_t)$, $t \in I$.

B.4 Finite element spaces

Let $\Omega_{h,t}$, $t \in I$ be a bounded domain triangulated by $\mathcal{T}_{h,t}$. Each triangular partition is known as an element S . We use barycentric coordinates as the local coordinate system on the elements of the triangulation. Let $\bar{\mathbb{P}}$ be a finite dimensional function space defined on \bar{S} , where \bar{S} is a reference element:

$$\bar{S} := \left\{ (\lambda_1, \dots, \lambda_3) \in \mathcal{R}^3; \, 0 \leq \lambda_i \leq 1, \, \sum_{i=1}^3 \lambda_i = 1 \right\}$$

then there exist a one-to-one mapping λ^S from \bar{S} to S . Let $w(\mathbf{x}(t))$ be a finite element function on an element S defined by a finite dimensional function space $\bar{\mathbb{P}}$ on a reference element \bar{S} and mapping λ^S from the reference element \bar{S} to S such that $w(\mathbf{x}(t)) = \bar{w}(\lambda^S(\mathbf{x}(t)))$, where \bar{w} is defined on \bar{S} . We define the space $\mathcal{X}^h(t) \subset H^1(\Omega_t)$:

$$\mathcal{X}^h(t) = \left\{ w \in C^0(\Omega_t); \, \bar{w} \in \bar{\mathbb{P}} \text{ for all } S \in \mathcal{T}_{h,t}, \, t \in I \right\}.$$

B.5 Finite element discretization of the model

We discretize problem (B.15) using the classical Galerkin method. At each time t , $t \in I$, we discretize Ω_t into a finite unstructured triangular partition $\Omega_{h,t}$ of non-overlapping triangles, where h is the maximum size of the largest triangle. Each triangular partition is known as an element S and the set of these finite triangular elements is called a mesh and is denoted by $\mathcal{T}_{h,t}$. Therefore

$$\bar{\Omega}_{h,t} = \bigcup_{S \in \mathcal{T}_{h,t}} S.$$

The discretized problem (P_S) of (B.15) reads: Find $a_h(\mathbf{x}, t)$, $u_h(\mathbf{x}, t)$, $v_h(\mathbf{x}, t) \in \mathcal{X}^h(t)$, $t \in I$ such that

$$\begin{aligned} \int_{\Omega_{h,t}} \frac{\partial w_h}{\partial x} \left(\mathbf{D}_{11} \frac{\partial \dot{u}_h}{\partial x} + \mathbf{D}_{12} \frac{\partial \dot{v}_h}{\partial y} + \mathbf{C}_{11} \frac{\partial u_h}{\partial x} + \mathbf{C}_{12} \frac{\partial v_h}{\partial y} \right) + \frac{\partial w_h}{\partial y} \left[\mathbf{D}_{33} \left(\frac{\partial \dot{u}_h}{\partial y} + \frac{\partial \dot{v}_h}{\partial x} \right) \right] \\ + \frac{\partial w_h}{\partial y} \left[\mathbf{C}_{33} \left(\frac{\partial u_h}{\partial y} + \frac{\partial v_h}{\partial x} \right) \right] d\Omega_t = - \int_{\Omega_{h,t}} f_1 \frac{\partial w_h}{\partial x} d\Omega_t + \int_{\partial\Omega_{h,t}} n_1 f_1 w_h ds, \end{aligned} \quad (\text{B.16a})$$

$$\begin{aligned} \int_{\Omega_{h,t}} \frac{\partial w_h}{\partial y} \left(\mathbf{D}_{12} \frac{\partial \dot{u}_h}{\partial x} + \mathbf{D}_{22} \frac{\partial \dot{v}_h}{\partial y} + \mathbf{C}_{12} \frac{\partial u_h}{\partial x} + \mathbf{C}_{22} \frac{\partial v_h}{\partial y} \right) + \frac{\partial w_h}{\partial x} \left[\mathbf{D}_{33} \left(\frac{\partial \dot{u}_h}{\partial y} + \frac{\partial \dot{v}_h}{\partial x} \right) \right] \\ + \frac{\partial w_h}{\partial x} \left[\mathbf{C}_{33} \left(\frac{\partial u_h}{\partial y} + \frac{\partial v_h}{\partial x} \right) \right] d\Omega_t = - \int_{\Omega_{h,t}} f_2 \frac{\partial w_h}{\partial y} d\Omega_t + \int_{\partial\Omega_{h,t}} n_2 f_2 w_h ds, \end{aligned} \quad (\text{B.16b})$$

$$\begin{aligned} \frac{d}{dt} \int_{\Omega_{h,t}} a_h w_h d\Omega_t + \int_{\Omega_{h,t}} (D_a \nabla a_h \cdot \nabla w_h + k_a a_h w_h) d\Omega_t = \int_{\Omega_{h,t}} k_a a_c w_h d\Omega_t \\ + \int_{\Omega_{h,t}} a \frac{D w_h}{Dt} d\Omega_t, \end{aligned} \quad (\text{B.16c})$$

for all $w_h(\mathbf{x}, t) \in \mathcal{X}^h(t)$, $t \in I$. Let nde represent the total number of degrees of freedom of the nodes for the finite element discretization. Also let the set

$$\left\{ \varphi_i(\mathbf{x}, t), \varphi_i(\mathbf{x}, t) \in \mathcal{X}^h(t) \subset H^1(\Omega_t), \quad i = 1, \dots, nde \right\} \quad (\text{B.17})$$

represent piecewise linear finite element nodal basis functions satisfying that

$$\varphi_i(\mathbf{x}_j, t) = \begin{cases} 1 & \text{if } i = j, \\ 0 & \text{if } i \neq j. \end{cases}$$

We seek to find the finite element numerical approximation $a_h(\mathbf{x}, t)$, $u_h(\mathbf{x}, t)$, $v_h(\mathbf{x}, t) \in \mathcal{X}^h(t) \subset \mathcal{X}(\Omega_t)$ expressed as linear combinations of the linear nodal basis functions φ_i of the form

$$\begin{aligned} a_h(\mathbf{x}, t) &= \sum_{i=1}^{nde} \mathbf{a}_i(t) \varphi_i(\mathbf{x}, t), \quad u_h(\mathbf{x}, t) = \sum_{i=1}^{nde} \mathbf{U}_i(t) \varphi_i(\mathbf{x}, t), \quad v_h(\mathbf{x}, t) \\ &= \sum_{i=1}^{nde} \mathbf{V}_i(t) \varphi_i(\mathbf{x}, t). \end{aligned} \quad (\text{B.18})$$

Lemma B.2 (Transport property of basis functions) *The finite element space on the discretized domain is a space of continuous piecewise linear functions whose nodal basis functions have the following property;*

$$\frac{D\varphi_j}{Dt} = 0. \quad (\text{B.19})$$

A proof of this theorem can be found in (Dziuk and Elliott 2007).

Semi-discrete finite element model of the FBE

In order to write the semi-discrete finite element approximation of the FBE in block matrices form, we substitute w_h by the basis function φ_j , ($j = 1, \dots, nde$), u_h and v_h by their corresponding values as given in (B.18) into (B.16a) and (B.16b), then the resulting semi-discrete system of algebraic equations can be written in compact-matrix-vector form:

$$\begin{bmatrix} [\mathbf{A}^{11}(t)] & [\mathbf{A}^{12}(t)] \\ [\mathbf{A}^{12}(t)]^T & [\mathbf{A}^{22}(t)] \end{bmatrix} \begin{Bmatrix} \{\frac{d\mathbf{U}}{dt}(t)\} \\ \{\frac{d\mathbf{V}}{dt}(t)\} \end{Bmatrix} + \begin{bmatrix} [\mathbf{B}^{11}(t)] & [\mathbf{B}^{12}(t)] \\ [\mathbf{B}^{12}(t)]^T & [\mathbf{B}^{22}(t)] \end{bmatrix} \begin{Bmatrix} \{\mathbf{U}(t)\} \\ \{\mathbf{V}(t)\} \end{Bmatrix} = \begin{Bmatrix} \{\mathbf{F}^1(t)\} \\ \{\mathbf{F}^2(t)\} \end{Bmatrix} \quad (\text{B.20})$$

where $\begin{Bmatrix} \{\mathbf{U}(t)\} \\ \{\mathbf{V}(t)\} \end{Bmatrix}$ are solutions of the finite element semi-discrete scheme (B.20). In (B.20) we denote by $\{\mathbf{U}(t)\} = (\mathbf{U}_1(t), \dots, \mathbf{U}_{nde}(t))$, $\{\mathbf{V}(t)\} = (\mathbf{V}_1(t), \dots, \mathbf{V}_{nde}(t))$, $\{\frac{d\mathbf{U}}{dt}(t)\} = (\frac{d\mathbf{U}_1}{dt}(t), \dots, \frac{d\mathbf{U}_{nde}}{dt}(t))$ and $\{\frac{d\mathbf{V}}{dt}(t)\} = (\frac{d\mathbf{V}_1}{dt}(t), \dots, \frac{d\mathbf{V}_{nde}}{dt}(t))$ vectors of the solutions and their derivatives. $[\mathbf{A}^{kl}(t)]$, $[\mathbf{B}^{kl}(t)]$, ($k, l = 1, 2$) and $\mathbf{F}(t) := (\{\mathbf{F}^1(t)\}, \{\mathbf{F}^2(t)\})^T$ are time dependent stiffness matrices and generalised force vector respectively.

The entries of the time dependent stiffness matrices and generalised force vector for ($i, j = 1, \dots, nde$) are defined by

$$\begin{aligned} \mathbf{A}_{ij}^{11}(t) &:= \int_{\Omega_{h,t}} \left(\mathbf{D}_{11} \frac{\partial \varphi_i}{\partial x} \frac{\partial \varphi_j}{\partial x} + \mathbf{D}_{33} \frac{\partial \varphi_i}{\partial y} \frac{\partial \varphi_j}{\partial y} \right) d\Omega_t, \\ \mathbf{A}_{ij}^{22}(t) &:= \int_{\Omega_{h,t}} \left(\mathbf{D}_{33} \frac{\partial \varphi_i}{\partial x} \frac{\partial \varphi_j}{\partial x} + \mathbf{D}_{22} \frac{\partial \varphi_i}{\partial y} \frac{\partial \varphi_j}{\partial y} \right) d\Omega_t, \\ \mathbf{A}_{ij}^{12}(t) &:= \mathbf{A}_{ji}^{21}(t) = \int_{\Omega_{h,t}} \left(\mathbf{D}_{12} \frac{\partial \varphi_i}{\partial x} \frac{\partial \varphi_j}{\partial y} + \mathbf{D}_{33} \frac{\partial \varphi_i}{\partial y} \frac{\partial \varphi_j}{\partial x} \right) d\Omega_t, \end{aligned}$$

with

$$\begin{aligned} \mathbf{B}_{ij}^{11}(t) &:= \int_{\Omega_{h,t}} \left(\mathbf{C}_{11} \frac{\partial \varphi_i}{\partial x} \frac{\partial \varphi_j}{\partial x} + \mathbf{C}_{33} \frac{\partial \varphi_i}{\partial y} \frac{\partial \varphi_j}{\partial y} \right) d\Omega_t, \\ \mathbf{B}_{ij}^{22}(t) &:= \int_{\Omega_{h,t}} \left(\mathbf{C}_{33} \frac{\partial \varphi_i}{\partial x} \frac{\partial \varphi_j}{\partial x} + \mathbf{C}_{22} \frac{\partial \varphi_i}{\partial y} \frac{\partial \varphi_j}{\partial y} \right) d\Omega_t, \\ \mathbf{B}_{ij}^{12}(t) &:= \mathbf{B}_{ji}^{21}(t) = \int_{\Omega_{h,t}} \left(\mathbf{C}_{12} \frac{\partial \varphi_i}{\partial x} \frac{\partial \varphi_j}{\partial y} + \mathbf{C}_{33} \frac{\partial \varphi_i}{\partial y} \frac{\partial \varphi_j}{\partial x} \right) d\Omega_t, \end{aligned}$$

and

$$\begin{aligned}\mathbf{F}_j^1(t) &:= - \int_{\Omega_{h,t}} f_1 \frac{\partial \varphi_j}{\partial x} d\Omega_t + \int_{\partial\Omega_{h,t}} n_1 f_1 \varphi_j ds, \\ \mathbf{F}_j^2(t) &:= - \int_{\Omega_{h,t}} f_2 \frac{\partial \varphi_j}{\partial y} d\Omega_t + \int_{\partial\Omega_{h,t}} n_2 f_2 \varphi_j ds.\end{aligned}$$

For convenience's sake, we denote

$$\begin{aligned}[\mathbf{A}(t)] &:= \begin{bmatrix} [\mathbf{A}^{11}(t)] & [\mathbf{A}^{12}(t)] \\ [\mathbf{A}^{12}(t)]^T & [\mathbf{A}^{22}(t)] \end{bmatrix}, \quad [\mathbf{B}(t)] := \begin{bmatrix} [\mathbf{B}^{11}(t)] & [\mathbf{B}^{12}(t)] \\ [\mathbf{B}^{12}(t)]^T & [\mathbf{B}^{22}(t)] \end{bmatrix}, \\ \{\mathbf{U}(t)\} &:= \begin{Bmatrix} \{\mathbf{U}(t)\} \\ \{\mathbf{V}(t)\} \end{Bmatrix}, \quad \left\{ \frac{d\mathbf{U}}{dt}(t) \right\} := \begin{Bmatrix} \left\{ \frac{d\mathbf{U}}{dt}(t) \right\} \\ \left\{ \frac{d\mathbf{V}}{dt}(t) \right\} \end{Bmatrix} \quad \text{and} \quad \{\mathbf{F}(t)\} := \begin{Bmatrix} \{\mathbf{F}^1(t)\} \\ \{\mathbf{F}^2(t)\} \end{Bmatrix}.\end{aligned}$$

And we rewrite the semi-discrete finite element model for the force balance equation (B.20) in the form

$$[\mathbf{A}(t)] \left\{ \frac{d\mathbf{U}}{dt}(t) \right\} + [\mathbf{B}(t)] \{\mathbf{U}(t)\} = \mathbf{F}(t). \quad (\text{B.21})$$

Remark B.3 We note that some entries of the block matrices $[\mathbf{A}]$ and $[\mathbf{B}]$ are non-symmetric matrices. These entries are $[\mathbf{A}^{12}]$, $[\mathbf{A}^{12}]^T$, $[\mathbf{B}^{12}]$ and $[\mathbf{B}^{12}]^T$. A square matrix, say X is a non-symmetric matrix if the entries x_{ij} of X , are such that

$$x_{ij} \neq x_{ji}.$$

Since some entries of the block matrices $[\mathbf{A}]$ and $[\mathbf{B}]$ are non-symmetric matrices then $[\mathbf{A}]$ and $[\mathbf{B}]$ are non-symmetric block matrices.

Semi-discrete finite element model of the RDE

In order to write the semi-discrete finite element approximation of the RDE in matrix-vector form, we substitute w_h by the basis function φ_j , ($j = 1, \dots, nde$) and a_h by its corresponding value as given in (B.18) into (B.16c). Then we apply the transport property of basis functions as given in Lemma B.2 (the transport property states that $D\varphi_j/Dt = 0$). Upon applying the transport property of basis functions we obtain the following semi-discrete system of algebraic equations which we have written in compact-matrix-vector form;

$$\frac{d}{dt} (\mathbf{M}(t) \{\mathbf{a}(t)\}) + (D_a \mathbf{K}(t) + k_a \mathbf{M}(t)) \{\mathbf{a}(t)\} = k_a a_c \mathbf{H}(t), \quad (\text{B.22})$$

where $\{\mathbf{a}\} = (\mathbf{a}_1, \dots, \mathbf{a}_{nde})$ are actin concentration solutions of the semi-discrete scheme (B.22). \mathbf{M} , \mathbf{K} and \mathbf{H} are time dependent mass matrices, stiffness matrices and force vector respectively.

The entries of the time dependent matrices and force vector are defined respectively as

$$\mathbf{M}_{ij}(t) := \int_{\Omega_{h,t}} \varphi_i \varphi_j d\Omega_t, \quad \mathbf{K}_{ij}(t) := \int_{\Omega_{h,t}} \nabla \varphi_i \cdot \nabla \varphi_j d\Omega_t, \quad \text{and} \quad \mathbf{H}_j(t) := \int_{\Omega_{h,t}} \varphi_j d\Omega_t.$$

B.5.1 Fully discrete scheme of the coupled problem

In order to obtain a fully discrete finite element model of the coupled problem, we consider a modified implicit finite differentiation formula for the time integration of the semi-discrete finite element model of the FBE and the RDE as given in (B.21) and (B.22) respectively. Thus the fully discrete finite element model of the coupled problem is given by

$$([\mathbf{A}(t^n)] + \Delta t [\mathbf{B}(t^n)]) \{\mathbf{U}\}^{n+1} = [\mathbf{A}(t^n)] \{\mathbf{U}\}^n + \Delta t \mathbf{F}(\mathbf{t}^n), \quad (\text{B.23a})$$

$$[(1 + \Delta t k_a) \mathbf{M}(t^{n+1}) + \Delta t (D_a \mathbf{K}(t^{n+1}))] \{\mathbf{a}\}^{n+1} = \mathbf{M}(t^n) \{\mathbf{a}\}^n + \Delta t k_a c_c \mathbf{H}(t^n), \quad (\text{B.23b})$$

where $\{\mathbf{U}\}^n$, $\{\mathbf{U}\}^{n+1}$ are the displacement solutions computed at time t^n and t^{n+1} respectively. And $\{\mathbf{a}\}^n$, $\{\mathbf{a}\}^{n+1}$ are the actin concentrations at time t^n and t^{n+1} respectively. For the numerical implementation, the initial data $\{\mathbf{U}\}^0$ and $\{\mathbf{a}\}^0$ are interpolated on the initial mesh $\Omega_{h,0}$. All integral are evaluated using Gauss numerical quadrature (Reddy 1993). At each time t , $t \in I$, we assemble the finite elements to obtain the system of linear algebraic equations (B.23). The system of linear algebraic equation (B.23a) is solved using a generalised minimal residual method (GMRES) (Saad and Schultz 1986) while that of (B.23b) is solved using a conjugate gradient method (CG) with diagonal preconditioner (Saad 2003; Hestenes and Stiefel 1952). The implementation of the numerical scheme was carried out in ALBERTA 2.0¹, a finite element toolbox written in C language.

B.6 Numerical algorithm

The fully discrete coupled problem is solved iteratively. We present here a numerical algorithm for the method.

B.7 Computation of the evolution of the domain

In order to track the evolution of the domain accurately, we specify a Lagrangian kinematic description of the domain. We assume that the displacement of the boundary of the domain occurs only in the direction that is normal to its non-deformed position. The displacement of the domain boundary at any time t corresponds to the solutions of the force balance equation $\mathbf{U}(\mathbf{x}, t)$ at the boundary which in turn are dependent on the local concentration of the actin filament $\mathbf{a}(\mathbf{x}, t)$ at any particular space and time.

¹ <http://www.alberta-fem.de>.

Algorithm 7.1 [Fully discrete scheme]

Initialise \mathbf{U}^0 and \mathbf{a}^0 . Set the time-step size to Δt .

FOR $n = 1, \dots, T_F$ with time-step size Δt **DO**
 Assemble $\mathbf{M}(t^n)$, $\mathbf{H}(t^n)$, $[\mathbf{A}(t^n)]$, $[\mathbf{B}(t^n)]$ and $\mathbf{F}(t^n)$.
 Solve for $\{\mathbf{U}\}^{n+1}$ in (B.23a).
 Compute the new domain from the value of $\{\mathbf{U}\}^{n+1}$
 Assemble $\mathbf{M}(t^{n+1})$ and $\mathbf{K}(t^{n+1})$ on the new domain.
 Solve for $\{\mathbf{a}\}^{n+1}$ in (B.23b).
END FOR

The displacement of the interior nodes of the mesh is chosen to be equal to the flow velocity $\boldsymbol{\beta}$ (i.e. $\boldsymbol{\beta} = \dot{\mathbf{x}}$). On the boundary we assume that $\boldsymbol{\beta} = \boldsymbol{\omega}_n := \partial \mathbf{U} / \partial t$, where \mathbf{U} is the displacement solution of the force balance equation.

Let Ω_{t^n} and $\Omega_{t^{n+1}}$ be the domain at time t^n and t^{n+1} respectively. If we consider a time interval $[t^n, t^{n+1}]$ and assume that the spatial coordinates of Ω_{t^n} and $\Omega_{t^{n+1}}$ are known. Then we can define a first order linear approximation of the flow velocity as follows:

$$\boldsymbol{\beta}(\mathbf{x}, t^n) = \frac{\mathbf{x}(t^{n+1}) - \mathbf{x}(t^n)}{\Delta t}, \quad (\text{B.24})$$

where $\Delta t = t^{n+1} - t^n$ defines the time-step. We define a linear approximation of the domain $\Omega_{t^{n+1}}$ such that

$$\mathbf{x}(t^{n+1}) = \mathbf{x}(t^n) + \Delta t \boldsymbol{\omega}_n(\mathbf{x}, t^n). \quad (\text{B.25})$$

By substituting the above expression for $\boldsymbol{\beta}(\mathbf{x}, t^n) := \boldsymbol{\omega}_n(\mathbf{x}, t^n)$ into (B.25) and given \mathbf{U}^{n+1} results in mesh movement. where \mathbf{U}^{n+1} is the displacement solution of the force balance equation at time t^n (and specifies the displacement of the domain at time t^n). A Lagrangian kinematic description of the interior nodes of the mesh is used thus (B.25) equally specifies the position of the interior nodes.

Remark B.4 We remark again that the computation of the displacement of the domain (as defined above) is substantially different from that of Stephanou et al. (2004) model.

References

- Abramowitz M, Stegun IA (1968) Handbook of mathematical functions with formulas, graphs, and mathematical tables. US Government Printing Office, Washington, DC
- Alt W, Tranquillo RT (1995) Basic morphogenetic system modeling shape changes of migrating cells: How to explain fluctuating lamellipodial dynamics. J Biol Syst 3:905–916
- Ambrosio L, Fusco N, Pallara D (2000) Functions of bounded variation and free discontinuity problems. Clarendon Press, Oxford
- Ananthakrishnan R, Ehrlicher A (2007) The forces behind cell movement. Int J Biol Sci 3:303–317

- Ananthakrishnan R, Gusk J, Käs J (2006) Cell mechanics: recent advances with a theoretical perspective. *Recent Res Dev Biophys* 5:39–69
- Barnhart EL, Lee KC, Keren K, Mogilner A, Theriot J (2011) An adhesion-dependent switch between mechanisms that determine motile cell shape. *PLoS Biol* 9(5):e1001059
- Bausch AR, Ziemann F, Boulbitch AA, Jacobson K, Sackmann E (1998) Local measurements of viscoelastic parameters of adherent cell surfaces by magnetic bead microrheometry. *Biophys J* 75:2038–2049
- Binamé F, Pawlak G, Roux P, Hibner U (2010) What makes cells move: requirements and obstacles for spontaneous cell motility. *Mol BioSyst* 6:648–661
- Bischofs I, Klein F, Lehnert D, Bastmeyer M, Schwarz U (2008) Filamentous network mechanics and active contractility determine cell and tissue shape. *Biophys J* 95:3488–3496
- Brebbia CA (1981) *Boundary element methods*. Springer, Berlin, Heidelberg, New York
- Chen H, Bernstein BW, Bamburg JR (2000) Regulating actin-filament dynamics in vivo. *Trends Biochem Sci* 25:19–23
- Clark RAF (1996) *The molecular and cellular biology of wound repair*. Plenum Press, New York
- Cross MC, Hohenberg PC (1993) Pattern formation outside of equilibrium. *Rev Mod Phys* 65:851–1112
- Crouch SL, Starfield AH (1983) *Boundary element methods in solid mechanics*. George Allen and Unwin, London
- Dayel MJ, Akin O, Landeryou M, Risca V, Mogilner A, et al (2009) In silico reconstitution of actin-based symmetry breaking and motility. *PLoS Biol* 7:e1000201. doi:10.1371/journal.pbio.1000201
- Dziuk G, Elliott CM (2007) Finite elements on evolving surfaces. *IMA J Numer Anal* 27:262–292
- Edelstein-Keshet L (2005) *Mathematical models in Biology*. Society for Industrial and Applied Mathematics, Philadelphia
- Fleischer F, Ananthakrishnan R, Eckel S, Schmidt H, Käs J, Svitkina V, Michael B (2007) Actin network architecture and elasticity in lamellipodia of melanoma cells. *New J Phys* 9:420
- George U (2011) *A numerical approach to studying cell dynamics*. PhD thesis, University of Sussex
- Gupton LS, Anderson KL, Kole TP, Fischer RS, Ponti A, Hitchcock-DeGregori SE, Danuser G, Fowler VM, Wirtz D, Hanein D, Waterman-Storer CM (2005) Cell migration without a lamellipodium: translation of actin dynamics into cell movement mediated by tropomyosin. *J Cell Biol* 168:619–631
- Hestenes MR, Stiefel E (1952) Methods of conjugate gradients for solving linear systems. *J Res Natl Bur Stand* 49:409–436
- Hofreither C, Langer U, Tomar S (2010) Large-scale scientific computing, 7th international conference, LSSC 2009. In: Lirkov I, Margenov S, Waśniewski J (eds) *Boundary element simulation of linear water waves in a model basin*. Springer-Verlag, Berlin, Heidelberg
- Johnson C (1987) *Numerical solution of partial differential equations by the finite element method*. Cambridge University Press, Cambridge
- Keren K, Theriot JA (2008) Biophysical aspects of actin-based cell motility in fish epithelial keratocytes. In: Lenz P (ed) *Cell motility; biological and medical physics, biomedical engineering*. Springer Science + Business Media, LLC, New York
- LaForce T (2006) Pe281 boundary element method course notes. <http://www.stanford.edu/class/energy281/BoundaryElementMethod.pdf>. Accessed May 2011
- Lanni F, Ware BR (1984) Detection and characterization of actin monomers, oligomers, and filaments in solution by measurement of fluorescence photobleaching recovery. *Biophys J* 46:97–110
- Lauffenburgy DA, Horwitz AF (1996) Cell migration: a physically integrated molecular process. *Cell* 84:359–369
- Le Clainche C, Carlier MF (2008) Regulation of actin assembly associated with protrusion and adhesion in cell migration. *Physiol Rev* 88:489–513
- Lewis MA, Murray JD (1991) Analysis of stable two-dimensional patterns in contractile cytotel. *J Non-linear Sci* 1:289–311
- Lewis MA, Murray JD (1992) Analysis of dynamic and stationary pattern formation in the cell cortex. *J Biol Syst* 31:25–71
- Madzvamuse A (2000) *A numerical approach to the study of spatial pattern formation*. PhD thesis, Exeter college, University of Oxford
- Madzvamuse A, Wathern AJ, Maini PK (2003) A moving grid finite element method applied to a model biological pattern generator. *J Comput Phys* 190:478–500
- Maeda YT, Inose J, Matsuo MY, Iwaya S, Sano M (2008) Ordered patterns of cell shape and orientational correlation during spontaneous cell migration. *PLoS ONE* 3:e3734

- Moreo P, Gaffney EA, Garca-Aznar JM, Doblaré M (2010) On the modelling of biological patterns with mechanochemical models: insights from analysis and computation. *Bull Math Biol* 72:400–431
- Murray JD (1993) *Mathematical Biology*. Springer-Verlag, Berlin
- Okeyo KO, Adachi T, Sunaga J, Hojo M (2009) Actomyosin contractility spatiotemporally regulates actin network dynamics in migrating cells. *J Biomech* 42(15):2540–2548
- Paluch E, Piel M, Prost J, Bornens M, Sykes C (2005) Cortical actomyosin breakage triggers shape oscillations in cells and cell fragments. *Biophys J* 89:724–733
- Paluch E, Sykes C, Prost J, Bornens M (2006) Dynamic modes of the cortical actomyosin gel during cell locomotion and division. *Trends Cell Biol* 16:5–10
- Pullarkat PA, Fernández A (2007) Rheological properties of the eukaryotic cell cytoskeleton. *Phys Rep* 449:29–53
- Purcell E (1977) Life at low reynolds number. *Am J Phys* 45:1–11
- Reddy JN (1993) *An introduction to the finite element method*. McGraw-Hill, New York
- Ridley AJ, Schwartz MA, Burridge K, Firtel RA, Ginberg MH, Borisy G, Parsons JT, Horwitz AR (2003) Cell migration: Integrating signal from front to back. *Science* 302:1704–1709
- Saad Y (2003) *Iterative methods for sparse linear systems*. Society for Industrial and Applied Mathematics, Philadelphia
- Sadd MH (2005) *Elasticity: theory, applications and numerics*, vol 2. Elsevier, North Holland
- Sadd Y, Schultz MH (1986) Gmres: a generalized minimal residual algorithm for solving nonsymmetric linear systems. *SIAM J Sci Stat Comput* 7:856–869
- Senju Y, Miyata H (2009) The role of actomyosin contractility in the formation and dynamics of actin bundles during fibroblast spreading. *J Biochem* 145(2):137–150
- Sethian JA (1996) *Level set methods: evolving interfaces in geometry, fluid mechanics, computer vision and materials sciences*. Cambridge University Press, Cambridge
- Simon JR, Gough A, Urbank E, Wang F, Lanni F (1988) Analysis of rhodamine and fluorescein-labeled f-actin diffusion in vitro by fluorescence photobleaching recovery. *Biophys J* 54:801–815
- Stephanou A (2010) *Spatio-temporal dynamics of the cell: characterization from images and computer simulations*. Lambert Academic Publishing, Victoria
- Stephanou A, Chaplain M, Tracqui P (2004) A mathematical model for the dynamics of large membrane deformations of isolated fibroblasts. *Bull Math Biol* 66:1119–1154
- Stéphanou A, Mylona E, Chaplain M, Tracqui P (2008) A computational model of cell migration coupling the growth of focal adhesions with oscillatory cell protrusions. *J Theor Biol* 253:701–716
- Strang G, Fix G (1988) *An analysis of the finite element method*, vol 2. Cambridge Press, Wellesley
- Watanabe N (2010) Inside view of cell locomotion through single-molecule: fast f-/g-actin cycle and g-actin regulation of polymer restoration. *Proc Jpn Acad* 86:62–83
- Xue F, Janzen DM, Knecht DA (2010) Contribution of filopodia to cell migration: a mechanical link between protrusion and contraction. *Int J Cell Biol* 2010(2010):13. doi:[10.1155/2010/507821](https://doi.org/10.1155/2010/507821)
- Yang L, Dolnik M, Zhabotinsky AM, Epstein IR (2002) Pattern formation arising from interactions between Turing and wave instabilities. *J Chem Phys* 117:7259–7265
- Zachmanoglou EC, Thoe DW (1986) *Introduction to partial differential equations with applications*. Dover Publications, Inc., New York
- Zaman MH, Kamm RD, Matsudaira P, Lauffenburger DA (2005) Computational model for cell migration in three-dimensional matrices. *Biophys J* 89:1389–1397
- Zhu C, Bao G, Wang N (2000) Cell mechanics: mechanical response, cell adhesion and molecular deformation. *Annu Rev Biomed Eng* 2:189–226
- Zienkiewicz OC (1977) *The finite element method*. McGraw-Hill, North Holland
- Zienkiewicz OC, Taylor RL, Zhu JZ (2005) *The finite element method: its basis and fundamentals*. Butterworth, Heinemann, Elsevier
- Zill DG, Cullen MR (2000) *Advanced engineering mathematics*. Jones and Bartlett Publishers International, Inc, London